Innexin function dictates the spatial relationship between distal somatic cells in the *Caenorhabditis elegans* gonad without impacting the germline stem cell pool

Theadora Tolkin*[1], Ariz Mohammad*[2], Todd Starich[3], Ken C. Q. Nguyen[4], David H. Hall[4], Tim Schedl[#,2], E. Jane Albert Hubbard[#,1,5,6], David Greenstein[#, 3]

[1] Kimmel Center for Biology and Medicine at the Skirball Institute, NYU Grossman School of Medicine, New York, NY, United States

[2] Department of Genetics, Washington University School of Medicine, St. Louis, MO, United States

[3] Department of Genetics, Cell Biology and Development, University of Minnesota, Minneapolis, MN, United States

[4] Department of Neuroscience, Albert Einstein College of Medicine, Bronx, NY 10461

[5] Department of Cell Biology, NYU Grossman School of Medicine, New York, NY, United States

[6] Department of Pathology, NYU Grossman School of Medicine, New York, NY, United States

*****equal contribution

co-corresponding

23

24 **Abstract**

25

26 Gap-junctional signaling mediates myriad cellular interactions in metazoans. Yet, how gap
27 junctions control the positioning of cells in organs is not well understood. Innexins compose gap
28 junctions in invertebrates and affect organ architecture. Here, we investigate the roles of gap-
29 junctions in controlling distal somatic gonad architecture and its relationship to underlying
30 germline stem cells in *Caenorhabditis elegans*. We show that a reduction of soma–germline
31 gap-junctional activity causes displacement of distal sheath cells (Sh1) towards the distal end of
32 the gonad. We confirm, by live imaging, transmission electron microscopy, and antibody
33 staining, that bare regions—lacking somatic gonadal cell coverage of germ cells—are present
34 between the distal tip cell (DTC) and Sh1, and we show that an innexin fusion protein used in a
35 prior study encodes an antimorphic gap junction subunit that mispositions Sh1. We determine
36 that, contrary to the model put forth in the prior study based on this fusion protein, Sh1
37 mispositioning does not markedly alter the position of the borders of the stem cell pool nor of
38 the progenitor cell pool. Together, these results demonstrate that gap junctions can control the
39 position of Sh1, but that Sh1 position is neither relevant for GLP-1/Notch signaling nor for the
40 exit of germ cells from the stem cell pool.

41

42

43

44 **Introduction**

45

46 The relative positions of certain cells within larger organ structures are often important for
47 tissue function. Yet the mechanisms by which cells reach and maintain their precise relative
48 positions within organs are poorly defined. Gap junctions act as conduits for small molecules
49 passed between cells and/or as rivets to ensure adhesion between cells (reviewed by (Skerrett
50 and Williams, 2017)). They have also been implicated in cell morphology within organs
51 (reviewed by (Phelan, 2005)), however this latter role is less well characterized. Here we take

advantage of well-characterized and stereotypical morphology, interactions, and relationships among cells in *Caenorhabditis elegans* to investigate the role gap junctions play in somatic gonad architecture and its consequences, or lack thereof, for the underlying germline stem cells.

The *C. elegans* hermaphrodite gonad provides a premier system for studying organogenesis and stem cell behavior (reviewed by (Hubbard and Greenstein, 2000; Hubbard and Schedl, 2019)). Two gonad arms, anterior or posterior of a central uterus and vulva, are each capped by a single somatic cell, the distal tip cell (DTC), that establishes a stem cell niche. Germline stem cells and their proliferative progeny, which together are referred to as progenitors, are maintained by GLP-1/Notch-mediated signaling in the germ line in response to DSL family ligands LAG-2 and APX-1 produced by the DTC (Austin and Kimble, 1987; Berry et al., 1997; Henderson et al., 1994; Nadarajan et al., 2009; Yochem and Greenwald, 1989). Proximal to the DTC, five pairs of sheath cells (named as pairs Sh1 to Sh5, distal to proximal) provide additional support to the germ line. In particular, Sh1 is implicated in promoting germline progenitor cell proliferation (Killian and Hubbard, 2005; McCarter et al., 1997). Although the molecular and cellular mechanisms by which Sh1 promotes germline proliferation remain to be fully elucidated, it is clear that one mechanism for the function of these cells involves the formation of gap junctions with germ cells (Starich et al., 2014).

Invertebrate gap junctions are formed from octameric hemichannels of innexin proteins (Oshima et al., 2016). In *C. elegans*, INX-8 and INX-9 associate to form hemichannels in the hermaphrodite somatic gonad which couple to germline innexin hemichannels (INX-14 with INX-21 or INX-22) to promote germline proliferation and inhibit meiotic maturation, respectively (Figure 1A–B; (Starich et al., 2014)). Phenotypic analysis of reduction-of-function mutants in *inx-8* recently led to the discovery of malonyl-CoA as a key cargo that traverses the soma-germline junctions to ensure proper embryogenesis (Starich et al., 2020) .

80 In the distal gonad, the somatic gonadal hemichannel components INX-8 and INX-9 are required
81 redundantly for germ cell proliferation and differentiation. Loss of both components renders
82 the germ line devoid of all but a handful of germ cells, which fail to undergo gametogenesis.
83 Restoration of *inx-8* either to the DTC or to sheath cells rescues the severe germline
84 proliferation defect of the *inx-8(0) inx-9(0)* double mutant (Starich et al., 2014). In addition, a
85 reduction of *inx-8* and *inx-9* via hypomorphic alleles or by RNA interference limits expansion of
86 the pool of proliferative germ cells (Dalfo et al., 2020; Starich and Greenstein, 2020; Starich et
87 al., 2014). The mutant innexin allele combinations used in this study are proficient in promoting
88 germline proliferation; however, as this work shows, many of them affect the position of Sh1
89 with respect to the distal end of the gonad.
90
91 Several prior observations point to a role for innexins in overall somatic gonad architecture. In
92 young adult hermaphrodites, the DTC forms long extending processes reaching proximally
93 towards Sh1, while the distal border of Sh1 is more regular, with filopodia extending distally
94 towards the DTC. Extensive ultrastructural and both fixed and live image analysis demonstrated
95 the existence of "bare regions" in between the proximal-extending DTC processes and the
96 distal-extending filopodial extensions of Sh1 in the adult hermaphrodite gonad. In these
97 regions, germ cells are in contact with neither the DTC nor Sh1, but are covered only by a basal
98 lamina ((Hall et al., 1999); Figure 1C and D). Interestingly, the hypomorphic allele *inx-14(ag17)*
99 (Miyata et al., 2008) causes Sh1 to reach almost to the distal end of the gonad (Starich et al.,
100 2014) and to obliterate any bare region between the DTC and Sh1. Similarly, a loss of bare
101 regions was observed in *inx-8(0) inx-9(0)* double mutants in which germline proliferation was
102 largely restored through expression of an *inx-8::gfp* transgene in the DTC only (Starich et al.,
103 2014). This latter result suggested that if Sh1 cannot form gap junctions with germ cells, Sh1
104 becomes distally mispositioned. However, the consequences of this mispositioning and the
105 accompanying loss of the bare regions for germline stem cells has not been previously
106 explored.
107

108 The spatial relationship between the DTC, Sh1 and the germ line summarized above was
109 recently challenged, and an hypothesis put forth that Sh1 might guide an oriented and
110 asymmetric division of stem cells, such that a daughter cell in contact with Sh1 enters the
111 differentiation pathway while the other, in contact with the DTC, remains a stem cell (Gordon
112 et al., 2020). If oriented cell fate-determining germ cell divisions occur in this way, the
113 expectation would be that germ cells undergoing such a division should be in contact with both
114 the DTC and Sh1, and that closely spaced daughter germ cells that have recently undergone
115 such a division would be remain in contact with one or the other. The model predicts that there
116 should be few if any germ cells that contact neither the DTC nor Sh1. If Sh1 drives cell fate-
117 determining germ cell divisions, another expectation would be that altering the position of Sh1
118 in the distal–proximal direction should similarly alter the position of the germline stem cell fate
119 decision. However, given that much of the analysis was performed using an INX-8 fusion protein
120 marker that could conceivably alter the position of Sh1, and given that the precise relationship
121 between the position of Sh1 vis-à-vis the border of the stem cell pool was not investigated, we
122 wished to determine how hypomorphic innexin alleles alter the position of Sh1 and whether
123 the position of Sh1 influences the germline stem or progenitor pools.
124
125 In short, we characterize the natural variability of Sh1 position and confirm the presence of
126 bare regions in gonads of early adult wild-type hermaphrodites. We show that reducing soma–
127 germline gap-junction coupling causes Sh1 to be mispositioned distally. In addition, we show
128 that the fusion protein used in the previous study (Gordon et al., 2020) encodes a dominant
129 antimorphic allele of *inx-8* that also causes distal mispositioning of Sh1. Finally, we determine
130 that when bare regions are absent due to Sh1 distal mispositioning, the borders of the stem or
131 progenitor cell pools are not markedly altered. Together, these results demonstrate that while
132 innexin function can dramatically impact the position of the distal border of Sh1, this position of
133 Sh1 is not relevant for GLP-1/Notch signaling nor for germ cells to exit the stem cell pool.
134
135
136 **Results**

137

138 **There is natural variability in the position of the distal border of Sh1, but gonads of wild-type**
139 **hermaphrodites display bare regions where germ cells contact neither the DTC nor Sh1**

140

141 As detailed below, we found that Sh1 is somewhat variably positioned in wild-type young adult
142 hermaphrodites. We confirmed the existence of bare regions between Sh1 and the DTC,
143 characterized by germ cells that do not contact Sh1 or the DTC.

144

145 To better characterize the natural variability in the position of the distal border of Sh1 in the
146 wild type, and to facilitate comparisons among different genotypes and markers, we binned
147 gonads into one of three phenotypic classes based on the position of Sh1 (Figure 1C–F; Video
148 1–3; Figure 1—figure supplement 1). To avoid ambiguity that results from the analysis of
149 maximum projection images, we analyzed all gonads in 3 dimensions (based on 0.5 µm optical
150 Z-series slices). We designated as Class 1, those gonads in which >8 µm (a distance covered by 2
151 germ cell diameters) separated the DTC and Sh1. Class 2 includes those gonads in which Sh1
152 and DTC processes come within 8 µm or in which Sh1 extensions intercalate with DTC
153 processes, up to the position of the mean length of DTC processes. Class 3 gonads are those in
154 which the border of Sh1 is markedly shifted distally such that it lies between the distal end of
155 the gonad and the mean DTC process length.

156

157 Using *bcIs39[lim-7p::ced-1::GFP]* to visualize Sh1, a transgene that produces a CED-1::GFP
158 fusion protein that fully rescues the sheath cell function of CED-1 to engulf germ cell corpses
159 (Zhou et al., 2001), we found that a majority of gonads (70%) are in Class 1, confirming the
160 existence of bare regions. Indeed, in many cases the distance between the proximal-most DTC
161 measurement and the distal-most Sh1 measurement exceeds 25 µm (Figure 1G; Figure 1—
162 figure supplement 1 panel D). The remaining gonads are in Class 2.

163

164 Using three additional Sh1 markers (and one alternate DTC marker), we found that depending
165 on the markers used, 50–90% of gonads fall into Class 1, while Class 2 make up the remainder

166 (Figure 1—figure supplement 1). We note that both Class 1 and Class 2 gonads contain bare
167 regions with spacing of germ cell nuclei (as seen by differential interference contrast
168 microscopy) such that their surrounding cell boundaries are not plausibly in contact with the
169 DTC or Sh1. We did not observe Class 3 gonads in any wild-type worms examined.
170
171 We also analyzed serial distal-to-proximal transmission electron micrographs (TEM) of a gonad
172 from a wild-type, unmarked young adult worm fixed using high-pressure freezing and freeze-
173 substitution freezing methods (Figure 1—figure supplement 2; Videos 4 and 5; Materials and
174 Methods). Focusing on an 80 µm region from the distal end to the distal extensions of Sh1, we
175 followed DTC processes (and their fragments) and Sh1 filopodial extensions among the tightly
176 packed germ cells (see Materials and Methods). We observed germ cells that contact neither a
177 DTC process (nor fragment thereof) nor filopodial extensions of Sh1, and thus represent bare
178 regions. Therefore, this TEM analysis is consistent with the confocal analysis above using cell
179 type-specific markers in live worms, and it corroborates prior ultrastructural observations made
180 on chemically fixed TEM preparations (Hall et al., 1999).
181
182
183 **Distal somatic gonad architecture is dictated by both somatic- and germline-expressed**
184 **innexins**
185
186 Previously, in fixed preparations, we observed that the distal edge of Sh1 was shifted nearly to
187 the distal end of the gonad in worms bearing a hypomorphic mutation in the germline innexin
188 *inx-14(ag17)* (Starich et al., 2014). We further investigated the position of Sh1 in *inx-14(ag17)*
189 using live imaging of intact young adult hermaphrodites bearing contrasting markers for Sh1
190 and the DTC (see Materials and Methods for details on markers used).
191
192 In contrast to *inx-14(+)*, the distal border of Sh1 in *inx-14(ag17)* extends to the distal end of the
193 gonad, well distal to the average position of the DTC processes (Figure 1C–E). The vast majority
194 of *inx-14(ag17)* gonads fall into Class 3 (Figure 1), with consistent results from three different

markers of Sh1 (Figure 1—figure supplement 1 panels B–E). Although our classification scheme references Sh1 relative to DTC position, we do not attribute this gross positional alteration of Sh1 to a change in the DTC. Instead, within strains with similar markers, the change in the *inx-14* genotype does not significantly change average DTC mean process length or the length of the longest DTC process, but it does have a significant effect on Sh1 distal border position (Figure 1G; Figure 1—figure supplement 1 panel E).

Table 1 Brood sizes and embryonic lethality measurements for selected strains

Strain	Relevant Genotype[a]	Brood (n)[b]	%Lethality (n)[c]	Sh1 mispositioned [d]
N2	Wild type	298.6 ± 42.1 (24)	0.4 ±0.4 (7194)	no
DG5063	*inx-8(qy78)*[e]	221.6 ± 23.6 (25)	9.0 ±4.6 (6087)	yes
NK2571	*inx-8(qy78); cpIs122*	212.8 ± 27.5 (23)	6.2 ±3.0 (5217)	(yes[f])
DG5059	*inx-9(ok1502)*	322.7 ± 33.0 (25)	0.2 ±0.3 (8081)	(no[f])
DG5064	*inx-8(qy102) inx-9(ok1502)*[g]	211.1 ± 47.2 (25)	1.1 ±1.1 (5327)	(yes[f])
NK2576	*inx-8(qy102) inx-9(ok1502); cpIs122*	209.5 ± 52.7 (23)	2.3 ±1.2 (4928)	(yes[f])
DG5250	*inx-8(qy78tn2031)*[h]	260.0 ± 25.9 (25)	0.1 ±0.2 (6504)	(no[f])
DG5251	*inx-8(tn2034)*[h]	301.6 ± 37.8 (25)	0.4 ±0.4 (7570)	(no[f])
DG5270	*inx-14(ag17)*	253.2 ± 28.1 (25)	0.4 ±0.6 (6356)	(yes[f])
DG5070	*inx-14(ag17); inx-8(qy78)*	106.6 ± 19.4 (25)	23.7 ±8.0 (3510)	n.d.
DG5380	*bcIs39*	282.6 ± 34.2 (25)	0.4 ±0.5 (7091)	n.d.
DG5020	*naIs37; bcIs39*	237.5 ± 46.5 (24)	1.0 ±1.4 (5753)	no
DG5320	*fasn-1(av138::gfp) naIs37*	342.4 ± 30.3 (25)	0.4 ±0.4 (8591)	no
DG5367	*inx-14(ag17) fasn-1(av138::gfp) naIs37*	256.0 ± 26.6 (23)	0.2 ±0.2 (5897)	yes
DG5378	*fasn-1(av138::gfp) naIs37; inx-8(qy78)*	245.4 ± 43.7 (23)	5.3 ±3.2 (5947)	yes

[a]Full genotypes in Supplementary File 1; genotypes *inx-8(qy78[mKate2::inx-8])* and *inx-8(qy102[mKate2::inx-8])* are abbreviated as "*inx-8(qy78)*" and "*inx-8(qy102)*" and *fasn-1(av138[fasn-1::GFP])* as *fasn-1(av138::gfp).*
[b]Brood size ± SD, n = number of broods counted
[c]Percent lethality ± SD, n = number of embryos scored
[d]yes/no indication of distal shift in the position of Sh1; relevant measurements in Figure 1, Figure 2, and their related supplements.
[e]Derived from NK2571 *inx-8(qy78); cpIs122 [lag-2p::mNeonGreen::plcdeltaPH]* (Gordon et al., 2020).
[f]These particular strains were not scored for Sh1 position. However, where equivalent *inx* genotypes were analyzed, the Sh1 phenotype is given in parenthesis; see Figure 1, Figure 2, and their related supplements.
[g]Derived from NK2576 *inx-8(qy102) inx-9(ok1502); cpIs122* (Gordon et al., 2020).
[h]Equivalent *inx-8(null)* CRISPR-Cas9 deletions generated in *inx-8(qy78[mKate2::inx-8])* or in wild-type genetic backgrounds.

To determine whether the position of Sh1 is shifted distally upon reduction of the somatic innexins, we investigated the position of Sh1 relative to the distal end of the gonad in a well-

238 characterized compound reduction-of-function (rf) *inx-8* mutant ((Starich et al., 2020); Figure
239 1B–G). We found that Sh1 in worms bearing one partially functional somatic gonad innexin
240 encoded by *inx-8(tn1513tn1555)* in an otherwise null *inx-9(ok1502)* background (hereafter
241 referred to as "*inx-8(rf)*"; (Starich et al., 2020)) is also distally positioned, similar to *inx-14(ag17)*
242 (Figure 1C–E). Thus, Sh1 is positioned distally as a result of reducing the function of either germ
243 line or somatic innexins in the distal gonad.
244
245
246 **An mKate2::INX-8 fusion causes a distal shift in the border of Sh1**
247
248 We extended our analysis to *inx-8(qy78[mKate2::inx-8])*, an allele that encodes an N-terminal
249 fusion protein of mKate2 and INX-8 that was used to mark Sh1 in a prior study ((Gordon et al.,
250 2020); Figure 2A). As detailed below, we found that—like *inx-14(ag17)* and *inx-8(rf)—inx-*
251 *8(qy78[mKate2::inx-8])* caused a distal shift in the position of Sh1 (Figure 2B–F). We
252 documented this shift both by anti-INX-8 antibody (Starich et al., 2014) detection in otherwise
253 unmarked strains (Figure 2B–C), as well as in live imaging of marked strains (Figure 2D–F).
254
255 We used anti-INX-8 antibody staining to compare the distal border of Sh1 in the unmarked wild
256 type and in *inx-8(qy78[mKate2::inx-8])* gonads (N2 and DG5063, respectively; see
257 Supplementary File 1; Figure 2—figure supplement 1). The mean distal boundary of INX-8
258 staining in the wild type lies at ~80 µm from the distal end of the gonad, while the mean distal
259 boundary of INX-8 staining in worms carrying *inx-8(qy78[mKate::inx-8)]* lies at ~50 µm from the
260 distal end, and the difference between these means is significant (Figure 2B–C). Moreover, in
261 89% of wild-type gonads (n=28), the distal border of Sh1 is greater than 60 µm (~15-16 cell
262 diameters) from the distal end of the gonad, while in 79% of *inx-8(qy78[mKate2::inx-8])* gonads
263 (n=32) the distal border of Sh1 is less than 60 µm from the distal end (Figure 2B–C).
264
265 Similar results were obtained using live imaging. Using *bcIs39* to visualize Sh1, no Class 3 gonads
266 (n=27) are observed in the wild type, compared to 65% (n=26) in *inx-8(qy78[mKate2::inx-8)]*

267 (Figure 2D–E). The same mKate2::INX-8 fusion, independently generated in an *inx-9(ok1502)*
268 null mutant background (i.e., *inx-8(qy102[mKate2::inx-8])*, see Materials and Methods, Gordon
269 et al., 2020), was also observed to shift Sh1 distally in *inx-8(qy102[mKate2::inx-8]) inx-*
270 *9(ok1502)* double mutants. In contrast, loss of *inx-9* alone does not significantly affect Sh1
271 position (Figure 2—figure supplement 2). If mKate::INX-8 were innocuous, the *inx-*
272 *8(qy102[mKate2::inx-8)]* allele in the absence of *inx-9* (*inx-9(1502)*) should have had no effect
273 on Sh1 position.
274
275 To explain the observed distal Sh1 border shift of mKate2::INX-8 compared to previous
276 descriptions of distal gonad architecture, Gordon et al. (2020) postulated that widely-used
277 markers of Sh1 driven by the *lim-7* promoter may not mark the entirety of the cell, excluding
278 the distal-most areas from detection. Although anti-INX-8 antibody staining clearly indicates a
279 more proximal position of Sh1 in otherwise unmarked wild-type strains and an evident distal
280 Sh1 shift in mKate2::INX-8, we wished to further determine whether the distal shift of Sh1 we
281 observed in *inx-8(qy78[mKate2::inx-8])* and *inx-14(ag17)* backgrounds reflected a disparity
282 between the expression patterns of mKate2::INX-8 and *lim-7p*-driven markers. First, we
283 consistently observe a dramatic distal shift of Sh1 in *inx-14(ag17)* using *lim-7* promoter-driven
284 transgenes (*bcIs39* and *tnIs5*) as well as using a functional endogenously tagged allele of the
285 fatty acid synthase gene *fasn-1*, [*fasn-1(av138[fasn-1::GFP])*] (Figure 1D; Figure 1—figure
286 supplement 1). We next examined the overlap between the mKate2::INX-8 and *lim-7p*-driven
287 markers in strains expressing both *inx-8(qy78[mKate2::inx-8])* and GFP markers encoded by
288 *tnIs6* [*lim-7p::gfp*] or *bcIs39* [*lim-7p::ced-1::gfp*]. In over 85% of gonad arms examined (n=20
289 and 26, respectively), the overlap between mKate2::INX-8 and GFP was complete (Figure 2—
290 figure supplement 3). In both *tnIs6* [*lim-7p::gfp*] or *bcIs39* [*lim-7p::ced-1::gfp*], the remaining
291 15% of gonads displayed either reduced Sh1 expression or expression in one, but not both, cells
292 of the Sh1 pair, which may result from stochastic transgene downregulation. Finally, we binned
293 these gonads into phenotypic Classes 1–3 based on measurements taken while observing either
294 mKate2 <u>*or*</u> GFP expression (Figure 2—Figure supplement 3 panel D). The number of Class 3
295 gonads is somewhat underestimated with the GFP markers. Nevertheless, we observe a marked

296 distal shift in the *inx-14* and *inx-8* mutants bearing these markers. In sum, if the GFP markers
297 were not marking the distal-most part of Sh1, we should not have been able to so readily detect
298 the abnormal distal displacement of Sh1 in *inx-14(ag17), inx-8(rf) or inx-8(qy78[mKate2::inx-8]*
299 strains bearing these markers.
300
301 We conclude that despite variability in the exact position of the Sh1 border, and despite minor
302 differences in transgene expression, bare regions between the Sh1 and the DTC are present in
303 the wild type, and they are greatly diminished due to a distal shift in the position of Sh1 in
304 worms bearing reduced *inx-14* or *inx-8* function or bearing the mKate2::INX-8 fusion.
305
306
307 **An mKate2::INX-8 fusion behaves as a dominant dosage-sensitive antimorph**
308
309 Based on our observations that *inx-8(qy78[mKate2::inx-8)])* gonads display a distally shifted
310 border of Sh1, we hypothesized that this allele might encode an INX-8 protein that poisons
311 innexin complexes thereby interfering with the channel and/or adhesion functions important
312 for Sh1 positioning. If this were due to a toxic effect of the mKate2::INX-8 fusion protein on gap
313 junctions, we would predict that the distal shift of Sh1 would be dependent on the presence of
314 the INX-8 coding region. To test this hypothesis, we used CRISPR-Cas9 genome editing to
315 generate *inx-8* null alleles in both the *inx-8(qy78[mKate2::inx-8])* and wild-type genetic
316 backgrounds. We generated deletions with identical breakpoints in the *inx-8* locus in both
317 genetic backgrounds [i.e., *inx-8(qy78tn2031)* and *inx-8(tn2034)*] starting 136 bp upstream of the
318 wild-type *inx-8* ATG start codon and extending 221 bp into *inx-8* exon 3 (Figure 2 and Figure 2—
319 figure supplement 2). In the *inx-8(qy78[mKate2::inx-8])* context, this deletion also removes the
320 mKate2 moiety. These deletions are expected to constitute *inx-8* null alleles because, in
321 addition to removing the start codon, they delete amino acids 1–349 (out of 382 amino acids),
322 including virtually all residues essential for spanning the plasma membrane and forming a
323 channel (Starich and Greenstein, 2020). Consistent with our hypothesis, the deletion mutant
324 *inx-8(qy78tn2031)* displays a significantly lower frequency of Class 3 gonads than the original

325 *inx-8(qy78[mKate2::inx-8])* allele. Sh1 in the *inx-8(qy78tn2031)* deletion mutant is positioned
326 more proximally, and therefore, like the wild type, exhibits bare regions that are lacking in *inx-*
327 *8(qy78[mKate2::inx-8])* mutants (Figure 2D–F). In addition, *inx-8(qy78tn2031)* exhibits a nearly
328 normal brood size and suppresses the low-level embryonic lethality observed in the *inx-8(qy78)*
329 starting strain (Table 1). Likewise, the identical deletion generated in the wild-type genetic
330 background, *inx-8(tn2034)*, also exhibits the wild-type Sh1 position (Figure 2—figure
331 supplement 2), with a normal brood size and negligible embryonic lethality (Table 1). However,
332 the observation of a small percentage of Class 3 gonads in *inx-8(qy78tn2031)* and *inx-8(tn2034)*
333 animals but not in the wild type (Figure 2—figure supplement 2), suggests that the position of
334 Sh1 is sensitive to the dosage of somatic gap junction hemichannels. In fact, the *inx-*
335 *8(qy78tn2031)/+* heterozygote reveals apparent haploinsufficiency for this phenotype (Figure
336 2—figure supplement 2).
337
338 We made several additional observations from a brood-size and embryonic-viability analysis
339 (Table 1). First, the marker transgenes do not have an appreciable effect on brood size or
340 embryonic lethality in our hands. Second, genetic interactions exist between *inx-*
341 *8(qy78[mKate2::inx-8], inx-14(ag17)* and the *inx-9(ok1502*) null mutation. Specifically, *inx-*
342 *14(ag17)* enhances both the reduced brood size and embryonic lethality of *inx-*
343 *8(qy78[mKate2::inx-8]*; whereas *inx-9(ok1502*) weakly suppresses the embryonic lethality
344 defect (Table 1). Third, in the course of this analysis, we noted that strains bearing *inx-*
345 *8(qy78[mKate2::inx-8]* displayed highly variable population growth dynamics that we attribute
346 to stress. Although the relevant stressor has yet to be determined, we observed this effect over
347 multiple generations after starvation or transport. Given our previous finding that key
348 metabolites such as malonyl-CoA are transported through these junctions to support
349 embryonic growth, this finding deserves future scrutiny.
350
351 Finally, to assess more fully the nature of the *inx-8(qy78[mKate2::inx-8]* allele with respect to
352 Sh1 position, we generated and imaged worms bearing this allele in heterozygous and
353 hemizygous configurations (Figure 2—figure supplement 2; we abbreviate *inx-*

354 *8(qy78[mKate2::inx-8]* to "*qy78*" and null to (0), below, to aid comparison between genotypes).
355 We infer loss-of-function behavior since other loss-of-function mutations affecting soma-
356 germline gap junctions, such as *inx-14(ag17),* also cause a distal shift in the Sh1 border.
357 Nevertheless, *inx-8(qy78)* is dominant: a substantial proportion of gonads in *qy78/+* are in Class
358 3, similar to *qy78/qy78,* but distinct from deletion heterozygotes [*inx-8(qy78tn2031/+*].
359 However, in a hemizygous configuration (*qy78/0*), the Sh1 distal displacement phenotype is
360 largely suppressed. Thus, *qy78* acts as a dosage-sensitive antimorph. We speculate that the
361 fusion protein produced by *inx-8(qy78[mKate2::inx-8])* can form dysfunctional junctions on its
362 own or with INX-8(+), but not when it is present below a certain abundance threshold. As also
363 mentioned above, the *inx-8* deletion allele *qy78tn2031*, while largely suppressing the Sh1 distal
364 mispositioning defect, displays a weak dominant haploinsufficient behavior consistent with
365 dosage sensitivity. Alternatively, this behavior could result from genetic positional effects that
366 impinge on nearby *inx-9* function and for which Sh1 position is particularly sensitive.
367
368 **The distal position of Sh1 does not influence the position of the stem cell pool border**
369
370 A recent model proposed that the position of the Sh1 border influences the stem/non-stem
371 decision in underlying germ cells (Gordon et al., 2020). However, because the previous study
372 did not examine the position of stem or progenitor cells, and because the model was based on
373 results using the antimorphic *inx-8(qy78[mKate2::inx-8])* allele, we investigated this
374 relationship.
375
376 In its simplest form, the model proposed by Gordon et al. (2020) predicts that when the distal
377 edge of Sh1 is positioned distally, the stem/non-stem border should similarly shift distally. The
378 SYGL-1 protein serves as a stem cell marker as *sygl-1* is a direct transcriptional target of GLP-
379 1/Notch in the germ line (Chen et al., 2020; Kershner et al., 2014; Lee et al., 2019; Lee et al.,
380 2016; Shin et al., 2017). We analyzed the proximal extent of the pool of SYGL-1-positive cells
381 bearing a well-characterized OLLAS epitope tag on SYGL-1 (Shin et al., 2017) and compared that
382 boundary relative to the distal Sh1 border (Figure 3 and Materials and Methods). In the case of

383 *inx-14(ag17),* though the distal border of Sh1 was shifted drastically and significantly, there was
384 no significant change in the position of the border of the SYGL-1-positive stem cell pool. In the
385 case of the *inx-8(qy78[mKate2::inx-8])* allele, the border of the SYGL-1-positive pool was
386 marginally shifted distally relative to the wild type, though not commensurate with the extent
387 to which Sh1 shifted distally in this background (Figure 3C). Furthermore, the marginal shift of
388 the border of the stem cell pool in *inx-8(qy78[mKate2::inx-8])* was suppressed when *inx-8* was
389 deleted in both *inx-8(qy78tn2031)* and *inx-8(tn2034)*. The marginal shift in the border of the
390 stem cell pool is not observed in *inx-14(ag17),* suggesting that such a defect in *inx-*
391 *8(qy78[mKate2::inx-8])* is due to the altered function of mKate2::INX-8, rather than the position
392 of Sh1 *per se* (Figure 3A-C). To detect any subtle correlation between the proximal border of
393 the SYGL-1 pool and the distal border of Sh1, we plotted these against one another and
394 computed an R value (Figure 3D). By Pearson correlation, there is no significant relationship in
395 any genotype examined between the position of the Sh1 border and the position of the SYGL-1-
396 positive stem cell pool border. There is no significant relationship regardless of whether
397 measurements are made in microns (Figure 3) or cell diameters (CD; Figure 3 and Figure 3—
398 figure supplement 1).
399
400 The recent model also proposed that Sh1 controls spindle orientation at the stem/progenitor
401 border. However, we found that in the wild-type (marker-only) strain, the distal border of Sh1
402 was proximal to the proximal SYGL-1-positive border in 86% of the gonads (n=320), with a
403 distance between them of ≥5 CD in 67% of the gonads (Figure 3 and Figure 3—figure
404 supplement 1). As mentioned above, this 5 CD distance is inconsistent with the hypothesis that
405 Sh1 is controlling spindle orientation at the stem cell border as such control would be expected
406 to occur over a distance of only 1–2 cell diameters.
407
408 We conclude that (1) there is no correlation between the position of the distal border of Sh1
409 and the proximal border of the SYGL-1-positive stem cell pool, and (2) if spindle-oriented
410 divisions occur at the Sh1 border, they are not influencing stem cell fate.
411

412

413 **The distal position of Sh1 does not influence the position of the progenitor pool border**

414

415 Although we found no correlation between the stem cell pool border and Sh1 position, we
416 wondered whether altered Sh1 position might nevertheless influence the position of the border
417 between the progenitor zone (PZ) and the transition zone that marks overt meiotic entry. In the
418 wild type, consistent with our previous analysis in live worms, we found that the distal position
419 of Sh1 is somewhat variable and can be either distal or proximal of the PZ border, using the
420 length of the CYE-1-positive region to define the PZ border, following CYE-1 and pSUN-1(S8) co-
421 staining (Figure 4 and Materials and Methods; Mohammad et al., 2018). We found that
422 although there is a subtle shift in the PZ border in *inx-8(qy78[mKate2::inx-8])* and *inx-14(ag17)*,
423 it does not correlate with the dramatic shift in Sh1 position seen in these mutants (Figure 4).
424 Again, we saw no significant correlation between Sh1 position and the position of the PZ border
425 (Figure 4D). As with the SYGL-1 analysis, the relationships are similar when measurements are
426 made in microns (Figure 4) or in CD (Figure 4—figure supplement 1), noting that differences
427 between genotypes are more apparent in the micron measurements since cells are slightly
428 larger more proximally in the PZ.

429 In sum, the border between the PZ and the transition zone is not markedly altered relative to
430 the dramatic distal displacement of the Sh1 border in *inx-14(ag17)* or in *inx-*
431 *8(qy78[mKate2::inx-8]*, suggesting that the position of Sh1 has no bearing on the position of
432 meiotic entry.

433

434

435 **Discussion**

436

437 These studies show that impaired innexin function distally mispositions Sh1, but that this
438 displacement does not similarly shift the proximal border of the stem cell pool (Figure 5). We

439 show that bare regions of variable size normally exist between the DTC and Sh1, in which germ
440 cells lack contact with the DTC or Sh1, but that these bare regions are diminished or lost with
441 reduced innexin activity either in the soma or the germ line. These findings offer a unified
442 explanation for a previous observation of loss of bare regions between the DTC and Sh1 in
443 strains carrying an mKate2::INX-8 fusion marker that, we now determine, is interfering with
444 innexin function. We concur with the previous observation: bare regions are lost in strains
445 carrying this fusion. The previous interpretation was that the mKate2::INX-8 was marking a
446 distal-most part of Sh1 that was not detectable with other markers. This led to a model
447 whereby Sh1 influences the stem cell fate decision in the underlying germ cells. Instead, we
448 show that the mKate2::INX-8 fusion itself alters innexin function such that Sh1 is distally
449 mispositioned and this mispositioning obliterates the bare regions. Our interpretation is
450 consistent with results obtained by TEM analysis (Hall et al., 1999; this work), antibody staining
451 (Starich et al., 2014; this work), and live imaging in strains bearing different fluorescent proteins
452 expressed in Sh1, as well as our genetic analysis. The cautionary tale is that fusion proteins used
453 as markers, even when they are generated by CRISPR/Cas9 genome editing in the context of
454 the endogenous locus—and therefore are not likely mis-expressed or overexpressed—may
455 nevertheless generate proteins that are not benign. Here, the mKate2::INX-8 fusion protein
456 caused a distal shift in the Sh1 position due to its apparent antimorphic effect on gap junctions.
457 Because of the redundant function of INX-9, we were able to remove the mKate2::INX-8 protein
458 entirely and effectively restore the bare region.
459
460 Our finding that the germline response to signaling from the DTC, as measured by expression of
461 the GLP-1/Notch target, SYGL-1, is independent of germline interactions with distal sheath cells
462 (Sh1) is consistent with several other observations. For example, males, which lack sheath cells
463 altogether, exhibit stem cell pools similar to those in the hermaphrodite (Crittenden et al.,
464 2019). In addition, the stem cell and progenitor pools are present in larval stages prior DTC
465 process elaboration (Byrd et al., 2014), when Sh1 is positioned several CD from the DTC,
466 precluding the possibility of a DTC–Sh1 handoff at these stages (Killian and Hubbard 2005).
467 Here, we observed that the distal border of Sh1 relative to the proximal stem cell border in the

468 wild type is ≥5 CD in the majority of gonads we examined. Thus, the previous model that Sh1
469 orients divisions of stem cells to direct their fate is also called into question by our results.
470 Finally, using alleles that dramatically alter the position of Sh1, we found no evidence
471 supporting the prediction that the stem/non-stem border is coincident with the Sh1 border.
472 Together, these results indicate that Sh1 is not involved in the germline stem-progenitor fate
473 decision.
474
475 Our studies also provide evidence that innexin gap junctions not only serve as communication
476 and adhesion junctions, but that in the context of an organ system, they contribute to the
477 positioning of cells relative to each other. How might gap junctions influence the relative
478 position of the DTC and Sh1 in the distal gonad arm? The DTC also forms gap junctions with
479 germ cells, which must be disassembled as germ cells enter the bare region, only to be
480 reassembled again when in contact with Sh1 (and then again with more proximally located
481 sheath cells Sh2–5). A detailed TEM analysis of the gonad (Hall et al., 1999) led to the
482 consideration that a constant interplay of association and dissociation likely also occurs
483 between Sh1 and the underlying germ cells that move proximally along the arm: as germ cell
484 flux continually moves germ cells towards the proximal end of the gonad, the Sh1 cells
485 presumably extend their filopodia distally and form new gap junction connections with
486 incoming germ cells. Otherwise, the bare region would increase in length along the distal-
487 proximal axis.
488
489 Our observation that loss of the bare regions correlates with only a relatively modest effect on
490 brood size (Table 1) raises the question of what, if any, biological significance the bare regions
491 might have. Because the innexins have multiple functions in germline development (Starich et
492 al., 2014, 2020; Starich and Greenstein, 2020), we are unable to ascribe the observed brood-
493 size reduction in strains lacking bare regions to the absence of the bare regions *per se*. Thus,
494 any potential roles for the bare regions vis-à-vis brood size and germline development will
495 require additional study.
496

497 To complement the role of gap junctions in promoting robust proliferation, the kinetics of gap
498 junction coupling between the somatic gonad and germ cells may play a role in determining the
499 strength of the interactions between the two cell types. Unlike sheath–oocyte junctions, which
500 form large plaques containing many functional gap junctions, the gap junctions formed in the
501 distal arm appear to represent looser associations of a few gap-junction channels (Starich et al.,
502 2014). Nonetheless, these associations may be sufficient to maintain adhesion with the
503 underlying germline, functioning like regularly spaced rivets, albeit dynamic and removeable
504 ones.
505
506 Disentangling the adhesive and channel functions of gap junctions is a complex issue. The
507 mutants used in this study are competent to form soma–germline gap junctions—without
508 these, germ cells fail to proliferate. However, they may form such junctions less efficiently than
509 their wild-type counterparts. For example, the pattern of localization of gap junction puncta in
510 *inx-8(rf)* and *inx-14(ag17)* appears more diffuse than in the wild type (Starich et al., 2014;
511 Starich et al., 2020). Alternatively or additionally, the mutant innexins in this study may
512 assemble into hemichannels as readily as wild-type innexins, but the pairing or opening of gap
513 junction channels may be compromised. Studies of connexin gap-junction channels in paired
514 *Xenopus* oocytes strongly suggest that opening of hemichannels facilitates their assembly into
515 gap junctions. That study proposed hemichannel opening collapses the intermembrane space
516 between juxtaposed cells to allow the extracellular loops of connexins to dock into gap
517 junctions (Beahm and Hall, 2004). If a similar model applies to innexin-containing gap junctions,
518 then rivet and channel function would be coupled.
519
520 How could impaired innexin function cause Sh1 to creep distally? One hypothesis is that when
521 fewer junctions are made, Sh1 cannot adhere as well to germ cells. This scenario would be
522 consistent with the observation that Sh1 is distally mispositioned when *inx-8* and *inx-9* are
523 missing from Sh1 but *inx-8(+)* is present in the DTC by virtue of heterologous expression of *inx-*
524 *8(+)* in the DTC in an *inx-8(0) inx-9(0)* double mutant (Starich et al., 2014). It is also possible that
525 the DTC and Sh1 engage in an active repellent or a passive space-excluding interaction that

526 somehow involves gap junction function. Another possibility is that a deficit in gap-junction
527 function might trigger Sh1 spreading as a means to increase the surface area over which
528 junctions may form to supply sufficient active biomolecules that transit through these
529 junctions. Nevertheless, our studies show that the position of germline stem cells is
530 independent of the position of Sh1.
531
532
533 **Acknowledgements**
534 We thank Gabriela Huelgas-Morales for discussions and constructive suggestions during the
535 course of this work, Swathi Arur for the affinity purified anti-GFP antibody, Verena Jantsch for
536 anti-pSUN-1 antibody, Edward Kipreos for anti-CYE-1 antibody. We thank Michael Cammer and
537 the NYU Langone Microscopy Core for experimental and technical support; the NYU Langone
538 Microscopy Laboratory is partially supported by the Cancer Center Support Grant P30CA016087
539 at the Laura and Isaac Perlmutter Cancer Center. We thank WormBase. We thank Kacy Gordon
540 and the CGC (which is funded by NIH Office of Research Infrastructure Programs P40
541 OD010440), for strains. NIH P30HD071593 and 1S10OD016214-01A1 supports electron
542 microscopy in DHH laboratory.
543
544
545 **References**
546
547 Arribere, J.A., Bell, R.T., Fu, B.X., Artiles, K.L., Hartman, P.S., Fire, A.Z., 2014. Efficient marker-
548 free recovery of custom genetic modifications with CRISPR/Cas9 in Caenorhabditis elegans.
549 Genetics 198, 837-846.
550
551 Austin, J., Kimble, J., 1987. glp-1 is required in the germ line for regulation of the decision
552 between mitosis and meiosis in C. elegans. Cell 51, 589-599.
553

554 Beahm, D.L., Hall, J.E., 2004. Opening hemichannels in nonjunctional membrane stimulates gap
555 junction formation. Biophys J 86, 781-796.
556
557 Berry, L.W., Westlund, B., Schedl, T., 1997. Germ-line tumor formation caused by activation of
558 glp-1, a Caenorhabditis elegans member of the Notch family of receptors. Development
559 (Cambridge, England) 124, 925-936.
560
561 Brodigan, T.M., Liu, J., Park, M., Kipreos, E.T., Krause, M., 2003. Cyclin E expression during
562 development in Caenorhabditis elegans. Dev Biol 254, 102-115.
563
564 Byrd, D.T., Knobel, K., Affeldt, K., Crittenden, S.L., Kimble, J., 2014. A DTC niche plexus
565 surrounds the germline stem cell pool in Caenorhabditis elegans. PLoS One 9, e88372.
566
567 Chen, J., Mohammad, A., Pazdernik, N., Huang, H., Bowman, B., Tycksen, E., Schedl, T., 2020.
568 GLP-1 Notch-LAG-1 CSL control of the germline stem cell fate is mediated by transcriptional
569 targets lst-1 and sygl-1. PLoS Genet 16, e1008650.
570
571 Cardona, A., Saalfeld, S., Schindelin, J., Arganda-Carreras, I., Preibisch, S., Longair, M.,
572 Tomancak, P., Hartenstein, V., Douglas, R. J., 2012. TrakEM2 software for neural circuit
573 reconstruction. PLoS One 7(6):e38011. doi: 10.1371/journal.pone.0038011.
574
575 Crittenden, S.L., Lee, C., Mohanty, I., Battula, S., Knobel, K., Kimble, J., 2019. Sexual dimorphism
576 of niche architecture and regulation of the Caenorhabditis elegans germline stem cell pool. Mol
577 Biol Cell 30, 1757-1769.
578
579 Dalfo, D., Ding, Y., Liang, Q., Fong, A., Cipriani, P.G., Piano, F., Zheng, J.C., Qin, Z., Hubbard,
580 E.J.A., 2020. A Genome-Wide RNAi Screen for Enhancers of a Germline Tumor Phenotype
581 Caused by Elevated GLP-1/Notch Signaling in Caenorhabditis elegans. G3 (Bethesda) 10, 4323-
582 4334.

583

584 Dejima, K., Hori, S., Iwata, S., Suehiro, Y., Yoshina, S., Motohashi, T., Mitani, S., 2018. An
585 Aneuploidy-Free and Structurally Defined Balancer Chromosome Toolkit for Caenorhabditis
586 elegans. Cell Rep 22, 232-241.
587
588 Dickinson, D.J., Ward, J.D., Reiner, D.J., Goldstein, B., 2013. Engineering the Caenorhabditis
589 elegans genome using Cas9-triggered homologous recombination. Nat Methods 10, 1028-1034.
590
591 Gordon, K.L., Zussman, J.W., Li, X., Miller, C., Sherwood, D.R., 2020. Stem cell niche exit in C.
592 elegans via orientation and segregation of daughter cells by a cryptic cell outside the niche. Elife
593 9.
594 Govindan, J.A., Nadarajan, S., Kim, S., Starich, T.A., Greenstein, D., 2009. Somatic cAMP
595 signaling regulates MSP-dependent oocyte growth and meiotic maturation in C. elegans.
596 Development 136, 2211-2221.
597
598 Hall, D.H., Hartwieg, E., Nguyen, K. C. Q, 2012. Modern Electron Microscopy Methods for *C.*
599 *elegans*. Methods in Cell Biol 107, 94-147.
600
601 Hall, D.H., Winfrey, V.P., Blaeuer, G., Hoffman, L.H., Furuta, T., Rose, K.L., Hobert, O.,
602 Greenstein, D., 1999. Ultrastructural features of the adult hermaphrodite gonad of
603 Caenorhabditis elegans: relations between the germ line and soma. Dev Biol 212, 101-123.
604
605 Henderson, S.T., Gao, D., Lambie, E.J., Kimble, J., 1994. lag-2 may encode a signaling ligand for
606 the GLP-1 and LIN-12 receptors of C. elegans. Development 120, 2913-2924.
607
608 Huang, L.S., Sternberg, P.W., 1995. Genetic dissection of developmental pathways. Methods
609 Cell Biol 48, 97-122.
610

611 Hubbard, E.J., Greenstein, D., 2000. The Caenorhabditis elegans gonad: a test tube for cell and
612 developmental biology. Dev Dyn 218, 2-22.
613
614 Hubbard, E.J.A., Schedl, T., 2019. Biology of the Caenorhabditis elegans Germline Stem Cell
615 System. Genetics 213, 1145-1188.
616
617 Kershner, A.M., Shin, H., Hansen, T.J., Kimble, J., 2014. Discovery of two GLP-1/Notch target
618 genes that account for the role of GLP-1/Notch signaling in stem cell maintenance. Proceedings
619 of the National Academy of Sciences.
620
621 Killian, D.J., Hubbard, E.J., 2005. Caenorhabditis elegans germline patterning requires
622 coordinated development of the somatic gonadal sheath and the germ line. Dev Biol 279, 322-
623 335.
624
625 Kocsisova, Z., Kornfeld, K., Schedl, T., 2019. Rapid population-wide declines in stem cell number
626 and activity during reproductive aging in C. elegans. Development 146.
627
628 Lee, C., Shin, H., Kimble, J., 2019. Dynamics of Notch-Dependent Transcriptional Bursting in Its
629 Native Context. Dev Cell 50, 426-435 e424.
630
631 Lee, C., Sorensen, E.B., Lynch, T.R., Kimble, J., 2016. C. elegans GLP-1/Notch activates
632 transcription in a probability gradient across the germline stem cell pool. eLife 5.
633
634 Lopez, A.L., Chen, J., Joo, H-J., Drake, M., Shidate, M., Kseib, C., Arur, S., 2013. DAF-2 and ERK
635 couple nutrient availability to meiotic progression during Caenorhabditis elegans oogenesis.
636 Dev Cell 27, 227-240.
637

638 McCarter, J., Bartlett, B., Dang, T., Schedl, T., 1997. Soma-germ cell interactions in
639 Caenorhabditis elegans: multiple events of hermaphrodite germline development require the
640 somatic sheath and spermathecal lineages. Developmental Biology 181, 121-143.
641
642 Miyata, S., Begun, J., Troemel, E.R., Ausubel, F.M., 2008. DAF-16-dependent suppression of
643 immunity during reproduction in Caenorhabditis elegans. Genetics 178, 903-918.
644
645 Mohammad, A., Vanden Broek, K., Wang, C., Daryabeigi, A., Jantsch, V., Hansen, D., Schedl, T.,
646 2018. Initiation of Meiotic Development Is Controlled by Three Post-transcriptional Pathways in
647 Caenorhabditis elegans. Genetics 209, 1197-1224.
648
649 Nadarajan, S., Govindan, J.A., McGovern, M., Hubbard, E.J., Greenstein, D., 2009. MSP and GLP-
650 1/Notch signaling coordinately regulate actomyosin-dependent cytoplasmic streaming and
651 oocyte growth in C. elegans. Development 136, 2223-2234.
652
653 Oshima, A., Tani, K., Fujiyoshi, Y., 2016. Atomic structure of the innexin-6 gap junction channel
654 determined by cryo-EM. Nat Commun 7, 13681.
655
656 Pekar, O., Ow, M.C., Hui, K.Y., Noyes, M.B., Hall, S.E., Hubbard, E.J.A., 2017. Linking the
657 environment, DAF-7/TGFbeta signaling and LAG-2/DSL ligand expression in the germline stem
658 cell niche. Development 144, 2896-2906.
659
660 Penkner, A.M., Fridkin, A., Gloggnitzer, J., Baudrimont, A., Machacek, T., Woglar, A., Csaszar, E.,
661 Pasierbek, P., Ammerer, G., Gruenbaum, Y., Jantsch, V., 2009. Meiotic chromosome homology
662 search involves modifications of the nuclear envelope protein Matefin/SUN-1. Cell 139, 920-
663 933.
664
665 Phelan, P., 2005. Innexins: members of an evolutionarily conserved family of gap-junction
666 proteins. Biochim Biophys Acta 1711, 225-245.

667

668 Shin, H., Haupt, K.A., Kershner, A.M., Kroll-Conner, P., Wickens, M., Kimble, J., 2017. SYGL-1 and
669 LST-1 link niche signaling to PUF RNA repression for stem cell maintenance in Caenorhabditis
670 elegans. PLoS Genet 13, e1007121.

671

672 Skerrett, I.M., Williams, J.B., 2017. A structural and functional comparison of gap junction
673 channels composed of connexins and innexins. Dev Neurobiol 77, 522-547.

674

675 Starich, T., Greenstein, D., 2020. A Limited and Diverse Set of Suppressor Mutations Restore
676 Function to INX-8 Mutant Hemichannels in the Caenorhabditis elegans Somatic Gonad.
677 Biomolecules 10.

678

679 Starich, T.A., Bai, X., Greenstein, D., 2020. Gap junctions deliver malonyl-CoA from soma to
680 germline to support embryogenesis in Caenorhabditis elegans. Elife 9.

681

682 Starich, T.A., Hall, D.H., Greenstein, D., 2014. Two classes of gap junction channels mediate
683 soma-germline interactions essential for germline proliferation and gametogenesis in
684 Caenorhabditis elegans. Genetics 198, 1127-1153.

685

686 Yochem, J., Greenwald, I., 1989. glp-1 and lin-12, genes implicated in distinct cell-cell
687 interactions in C. elegans, encode similar transmembrane proteins. Cell 58, 553-563.

688

689 Zhou, Z., Hartwieg, E., Horvitz, H.R., 2001. CED-1 is a transmembrane receptor that mediates
690 cell corpse engulfment in C. elegans. Cell 104, 43-56.

691

692

693 **Materials and Methods**

694

695 *Live imaging and image analysis of live samples*

696

697 Live specimens were grown at 20°C, and staged by picking mid-L4 larvae, then allowing them to
698 grow at 20°C until imaging them 24 hours later. Animals were immobilized using 10mM
699 Levamisole (Sigma T1512) in M9 buffer. Imaging was carried out on a Nikon W1 spinning disk
700 confocal microscope. We define a biological replicate as any set of individuals collected,
701 processed and imaged together. Numbers of individuals included in each analysis is indicated in
702 the figure legends.
703
704 Image analysis was carried out on 2-dimensional maximum-projection Z-stack images of 3D
705 confocal data. The distance from the distal end of the gonad to the end of each DTC process
706 was measured along a line drawn from the end of each process parallel to the distal-proximal
707 axis to a line drawn tangent to the distal end, orthogonal to the distal-proximal axis line (Figure
708 1—figure supplement 1). The distance between the distal end of the gonad and the most distal
709 extent of Sh1 was measured in the same way. All data points were recorded for each sample
710 and used to calculate the mean values presented in Figures 1 and 2 and related figure
711 supplements.
712
713 Sh1 visualization in live worms: *bcIs39* [*lim-7p*::CED-1::GFP] (Zhou et al., 2001) encodes a
714 functional membrane-localized fusion to CED-1. *tnIs5* and *tnIs6* encode an identical non-
715 functional fusion to the first 61 amino acids of LIM-7 (*tnIs5* or *tnIs6*) denoted here as "*lim-*
716 *7p*::GFP" that includes 2.23 kb upstream, the first two exons, and the first intron of *lim-7* fused
717 to GFP (Hall et al., 1999). *inx-8(qy78[mKate2::inx-8])* is an N-terminal fusion of mKate2 to INX-8
718 generated by CRISPR-Cas9 genome editing (Gordon et al., 2020*). fasn-1(av138[fasn-1::gfp])* was
719 generated by fusing GFP to the C-terminus of FASN-1 using CRISPR-Cas9 genome editing
720 (Starich et al., 2020). *tnEX42[acy-4::gfp + rol-6(su1006)]* contains GFP fused to the ACY-4 C-
721 terminus by recombineering in the fosmid WRM061bE10 (Govindan et al., 2009). ACY-4::GFP
722 rescues the sterility of *acy-4(ok1806)* null mutants via its function in the gonadal sheath cells.
723
724

725 DTC visualization in live worms: *naIs37*[*lag-2p*::mCherry-PH] encodes mCherry fused to the PH
726 domain of rat phospholipase C delta (Pekar et al., 2017) and *qIs154*[*lag-2p*::MYR-tdTomato]
727 encodes a src kinase myristoylation sequence fused to tdTomato (Byrd et al., 2014).
728
729 *Imaris rendering of confocal images*
730
731 3D rendering of confocal stacks for Videos 1–3 was done using Imaris (Oxford Instruments, plc.
732 Abingdon, UK) according to the following algorithm for batch processing. For the Sh1 channel
733 (green): Enable Smooth = true; Surface Grain Size = 0.433 µm; Enable Eliminate Background =
734 false; Diameter Of Largest Sphere = 1.63 µm; Enable Automatic Threshold = false; Manual
735 Threshold Value = 650; Active Threshold = true; Enable Automatic Threshold B = true; Manual
736 Threshold Value B = 31622.8. For the DTC channel (red): Enable Smooth = true; Surface Grain
737 Size = 0.433 µm; Enable Eliminate Background = false; Diameter Of Largest Sphere = 1.63 µm;
738 Enable Automatic Threshold = false; Manual Threshold Value = 710; Active Threshold = true;
739 Enable Automatic Threshold B = true; Manual Threshold Value B = 14988.5.
740
741 *Strains*
742
743 *C. elegans* strains (Supplementary File 1) were grown on standard NGM media with OP50 as a
744 food source (Brenner 1974) for all figures in this work. Strain constructions employed a
745 modified NGM medium [containing 6.25 µg/ml Nystatin and 12.5 mM potassium phosphate pH
746 6.0 (added after autoclaving) and 200 mg/ml streptomycin sulphate (added before
747 autoclaving)] with *E. coli* strain OP50-1 as food source. Strains were grown at 20°C. In addition
748 to the wild-type strain N2, the following alleles, described in WormBase (www.wormbase.org)
749 or in the cited references, were used:
750 Chr. I—*dpy-5(e61)* (Brenner 1974), *inx-14(ag17)* (Miyata et al., 2008; Starich et al., 2014), *unc-*
751 *13(e51)* (Brenner 1974), *fasn-1(av138[fasn-1::gfp])* (Starich et al. 2020), *sygl-*
752 *1(q983[3xOLLAS::sygl-1])* (Shin et al., 2017), *unc-54(e190)* (Brenner 1974).

753 Chr. IV—*inx-8(qy78[mKate2::inx-8])* (Gordon et al., 2020) , *inx-8(qy78 tn2031)* (this work), *inx-*
754 *8(tn2034)* (this work), *inx-8(tn2075)* (this allele was generated on the *tmC5* balancer
755 chromosome, this work), *inx-9(ok1502), inx-8(qy102[mKate2::inx-8)] inx-9(ok1502)* (Gordon et
756 al., 2020), *inx-8(tn1513tn1553) inx-9(ok1502)* (Starich and Greenstein, 2020), *inx-*
757 *8(tn1513tn1555) inx-9(ok1502)* (Starich et al., 2020), *dpy-20(e1282)* (Hosono et al. 1982).
758 Chr. V—*acy-4(ok1806)* (Govindan et al. 2009).
759 Balancer chromosomes (Dejima et al., 2018) used included: *tmC18 [dpy-5(tmIs1236)]* I,
760 *tmC27[tmIs1239]* I, *tmC5[tmIs1220]* IV.
761 Integrated transgenes included: *naIs37[lag-2p::mCherry::plcdeltaPH + unc-119(+)]* I (Pekar et
762 al., 2017), *mIs11[myo-2p::gfp + pes-10p::gfp + gut promoter::gfp]* IV, *bcIs39[lim-7p::ced-1::gfp +*
763 *lin-15(+)]* V (Zhou *et al*., 2001), *qIs154[lag-2p::MYR::tdTomato +ttx-3p::gfp]* V (Byrd et al., 2014),
764 *tnIs5[lim-7p::gfp + rol-6(su1006)]* X*, tnIs6[lim-7p::gfp + rol-6(su1006)]* X (Hall et al., 1999),
765 *cpIs122[lag-2p::mNeonGreen::plcdeltaPH]* (Gordon et al., 2020).
766 Extrachromosomal arrays used included: *tnEx42[acy-4::gfp + rol-6(su1006)]* (Govindan et al.,
767 2009).
768
769 *Strain constructions*
770
771 Multiply mutant strains were constructed in a straightforward manner (Huang and Sternberg,
772 1995). *tmC18* was used as a balancer chromosome for *inx-14(ag17)*. *tmC27* was used as a
773 balancer chromosome for *sygl-1(q983)*. *tmC5* (or the derivatives described) or *mIs11* were used
774 as balancer chromosomes for *inx-8* and *inx-9* mutant alleles. The presence of *inx-14(ag17)* in
775 strains was verified by PCR and DNA sequencing. The *ag17* allele was originally described as an
776 Arg to His change in the second extracellular loop of INX-14, but the exact residue position was
777 not specified (Miyata et al., 2008). A 1.2-kb PCR fragment covering this region was amplified
778 with primers inx-14delF and inx-14delR (see Supplementary File 2 for the sequence of
779 oligonucleotides used in this study). The PCR fragment was sequenced with the inx-14delR
780 primer. No sequence changes were found in Arg residues predicted to occupy the second
781 extracellular loop. However, a CGT to CAT (R326H) change was identified at a residue position

782 predicted to lie near the cytoplasmic end of the fourth transmembrane domain, and we
783 surmise that this change represents the original *ag17* mutation. The presence of the *sygl-*
784 *1(q983[3xOLLAS::sygl-1])* mutation in strains was verified by PCR with primers sygl1-F and sygl1-
785 R, which produce a 216 bp product in the wild type and a 348 bp product in *sygl-1(q983)* and by
786 anti-OLLAS staining. The presence of *inx-8(qy78tn2031)* and *inx-8(tn2034)* in strains was verified
787 by PCR with oligonucleotide primers inx8_delta.F and inx8_delta.R. To construct DG5367 *inx-*
788 *14(ag17) fasn-1(av138[fasn-1::gfp]) naIs37 I, fasn-1(av138[fasn-1::gfp]) naIs37/dpy-5(e61) unc-*
789 *13(e51)* heterozygotes were generated and Dpy non-Unc recombinants were sought, which
790 resulted in the isolation of a *dpy-5(e61) fasn-1(av138[fasn-1::gfp]) naIs37 I* intermediate strain.
791 From, *inx-14(ag17)/dpy-5(e61) fasn-1(av138[fasn-1::gfp]) naIs37* heterozygotes, recombinants
792 of genotype *inx-14(ag17) fasn-1(av138[fasn-1::gfp]) naIs37/dpy-5(e61) fasn-1(av138[fasn-*
793 *1::gfp]) naIs37* were identified by virtue of their increased GFP signal using a fluorescence
794 dissecting microscope. The presence of *inx-14(ag17)* in the desired recombinants was verified
795 by DNA sequencing. *naIs37* was shown to be tightly linked to *unc-54(e190)* on the right end of
796 LGI as follows. From *dpy-5(e61) fasn-1(av138[fasn-1::gfp]) naIs37/unc-54(e190)* heterozygotes,
797 of 15 *unc-54(e190)* homozygotes, none contained the *naIs37* marker (4 were recombinants
798 expressing *fasn-1::gfp*). Of 38 wild-type segregants of the aforementioned parental
799 heterozygous strain, all expressed the *naIs37* marker (11 were recombinants lacking *fasn-1::gfp*
800 expression). DG5380 was derived from DG5020 by crossing to N2 males and segregating away
801 *naIs37*; the *bcIs39* source was MD701, available from the CGC.
802
803 *Electron microscopy methods and analysis*
804
805 Wild-type N2 young adults were analyzed using high-pressure freezing/freeze-substitution
806 freezing (HPF/FS; Hall et al., 2012). Four animals from chemical immersion and four animals
807 from HPF/FS were collected in serial sections on slot grids, ranging from 80 nm–100 nm
808 thickness on an RMC PowerTome XL ultramicrotome (Eden Instruments, Valence, France).
809 Sections were post-stained in 2% uranyl acetate in H_2O for 20 min and in Reynold's lead for 3
810 min. Sections from each animal were viewed in the gonad region using Digital Micrograph

811 software (Gatan, Pleasanton, CA) for the JEOL JEM-1400Plus M (Jeol USA, Peabody, MA), using
812 a Gatan Orius SC1000B digital camera.
813
814 We selected the most optimally positioned and resolved HPF/FS-fixed animal (2% osmium
815 tetroxide, 0.1% uranyl acetate, and 2% H_2O in acetone) to collect high-resolution montages of
816 the gonad arm from every third section covering 80 µm, including the DTC and sheath filopodia
817 of a posterior distal gonad arm. This series was collected from the tail to the vulva region to
818 encompass the whole posterior gonad arm, but we did not collect full images closer to the
819 gonad reflection in order to save effort and expense. The pixel size for the images was 3.23 nm.
820 The images were aligned with TrakEM2 software (Cardona et al., 2012) and traced on a Wacom
821 DTZ 2100D tablet (Wacom, Portland, OR) to build the 3D model.
822
823 We followed the DTC processes and their fragments and the filopodial extensions of Sh1 due to
824 their increased translucency compared with the germ cells and by the fact that these somatic
825 cellular extensions contained many small mitochondria (Video 4). We observed what we infer
826 to be shed pieces of the DTC beginning at approximately 30 µm from the distal end, as has been
827 observed using light microscopic methods (Byrd et al., 2014). However, some DTC and Sh1
828 processes may appear discontinuous due to the fact that micrographs of every third section
829 were used to generate the reconstructed model (Video 5). Regardless of the effect that this
830 sampling technique has on our ability to resolve contiguous versus shed bits of somatic gonadal
831 cells, this TEM analysis is in agreement with our light microscopic observations that a large
832 subset of distal germ cell progenitors are not in contact either with the DTC or Sh1.
833
834 *Brood counts and embryonic lethality measurements*
835
836 Because *inx-8(qy78[mKate2::inx-8])* brood counts and embryonic lethality were highly variable,
837 we used a single batch of NGM media with OP50 food source for all brood count measurements
838 reported in Table 1. To prevent mold formation, the medium contained 6.25 µg/ml Nystatin. L4-
839 stage hermaphrodites were cultured individually on 35 mm Petri plates and transferred

840 approximately every 24 hours until they stopped producing embryos (4–6 days). Worms that
841 crawled off the media and died were redacted (varied from 0–10% depending on the
842 experiment). Embryos that failed to hatch after 24–36 hours were counted and scored as dead.
843 In the majority of cases, these embryos exhibited morphological abnormalities. Control
844 experiments demonstrated that these embryos were not simply delayed and never hatched.
845 Embryos that hatched were counted and scored as viable.
846
847 *Genome editing*
848
849 CRISPR-Cas9 genome editing was used to generate *inx-8* null alleles in both the *inx-*
850 *8(qy78[mKate2::inx-8])* and wild-type genetic backgrounds. The approach taken generated
851 identical 1525 bp deletions within the *inx-8* locus in both genetic backgrounds starting 136 bp
852 upstream of the wild-type *inx-8* ATG start codon and extending 221 bp into *inx-8* exon 3. In the
853 *inx-8(qy78[mKate2::inx-8])* context, this edit removes both the mKate2 moiety and *inx-8*. The
854 deletions are expected to constitute *inx-8* null alleles because, in addition to removing the start
855 codon, they delete amino acids 1–349 (out of 382 amino acids), including virtually all residues
856 essential for spanning the plasma membrane and forming a channel (Starich and Greenstein,
857 2020). The approach used pRB1017 to express two single guide RNAs (sgRNAs) under control of
858 the *C. elegans* U6 promoter (Arribere et al., 2014). Oligonucleotides inx8_us_sgRNA1.F and
859 inx8_us_sgRNA1.R were annealed and used to generate the plasmid inx8_us_sgRNA1 to direct
860 Cas9 cleavage 136 bp upstream of the ATG initiator codon (Supplementary File 2 lists all
861 oligonucleotides used in this study). Oligonucleotides inx8_sgRNA1.F and inx8_sgRNA1.R were
862 annealed and used to generate the plasmid inx8_sgRNA1 to direct Cas9 cleavage in exon 3. To
863 generate sgRNA clones, annealed oligonucleotides were ligated to *Bsa*I-digested pRB1017
864 plasmid vector, and the resulting plasmids were verified by Sanger sequencing. pDD162 served
865 as the source of Cas9 expressed under control of the *eef-1A.1/eft-3* promoter (Dickinson et al.,
866 2013). The repair template oligonucleotide used was inx8_rpr. Genome editing employed the
867 *dpy-10* co-conversion method (Arribere et al., 2014). The injection mix contained pJA58 (7.5
868 ng/µl), AF-ZF-827 (500 nM), inx8_us sgRNA1 (25 ng/µl), inx8_sgRNA1 (25 ng/µl), inx8_rpr (500

869 nM), and pDD162 (50 ng/µl) and was injected into adult hermaphrodites from strains DG5131
870 *naIs37[lag-2p::mCherry::PH + unc-119(+)] I; inx-8(qy78[mKate2::inx-8]) IV; bcIs39[lim-7p::ced-*
871 *1::gfp + lin-15(+)] V* and DG5020 *naIs37[plag-2::mCherryPH + unc-119(+)] I; bcIs39[lim-7p::ced-*
872 *1::gfp + lin-15(+)]V*. Correct targeting was verified by conducting PCR with primer pairs
873 inx8_delta.F and inx8_delta.R followed by DNA sequencing. Three deletion alleles were
874 recovered from the injections into DG5131 *(qy78tn2031, qy78tn2032,* and *qy78tn2033)*, and
875 two deletion alleles were recovered from the injections into DG5020 *(tn2034* and *tn2035)*. The
876 deletion alleles were outcrossed to *naIs37[lag-2p::mCherryPH +unc-119(+)]/+ I;*
877 *tmC5(tmIs1220[myo-2p::Venus])/+ IV; bcIs39[lim-7p::ced-1::gfp + lin-15(+)/+ V* males to
878 generate DG5229 and DG5232. Homozygous strains were analyzed by confocal microscopy. To
879 introduce an *inx-8* null allele onto the *tmC5[tmIs1220]* IV balancer chromosome, the same
880 injection mix of CRISPR reagents as described above was injected into *dpy-*
881 *20(e1282)/tmC5[tmIs1220]* IV heterozygotes. The *inx-8(tn2075)* null allele was generated on
882 the balancer chromosome, which resulted from a 1526 bp deletion that differed from the other
883 CRISPR-generated *inx-8* null alleles by the removal of an extra base at the cut site.
884
885 *Immunostaining and image analysis of fixed samples*
886
887 Immunostaining was carried out as described (Mohammad et al., 2018). Briefly, synchronized
888 adult hermaphrodites, 24-hr past mid-L4, were dissected in PBST (PBS with 0.1% Tween 20),
889 with 0.2 mM levamisole to extrude the gonads. The gonads were fixed in 3% paraformaldehyde
890 solution for 10 min and then post-fixed in −20° chilled methanol for 10 min. After 3x 10-min
891 washes with PBST, they were blocked in 30% goat serum for 30 min at RT. The gonads were
892 then incubated with the desired primary antibodies diluted (see below) in 30% goat serum at 4°
893 overnight. The next day, after 3x 10-min PBST washes, the gonads were further incubated with
894 appropriate secondary antibodies, diluted in 30% goat serum, at 4° overnight. The gonads were
895 washed 3 times with PBST, then incubated with 0.1 g/ml DAPI in PBST for 30 min. After removal
896 of excess liquid, the gonads were mixed with anti-fading agent (Vectashield) and transferred to
897 an agarose pad on a slide. Hyperstack images were captured using a spinning disk confocal

898 microscope (PerkinElmer-Cetus, Norwalk, CT). Two overlapping hyperstack images were
899 captured for each gonad arm to obtain coverage of >50 cell diameters from the distal end of
900 the gonad. Images were further processed in Fiji, and DAPI stained nuclei were used to mark
901 the number of cell diameters from the distal end. Employing pixel to micron ratio, specific to
902 the images captured, cell diameters were converted into microns where required.
903
904 SYGL-1-positive zone length assessment: OLLAS staining was used to assess 3xOLLAS::SYGL-1
905 accumulation (Shin et al., 2017). In wild-type young adults, SYGL-1 accumulates at the distal end
906 of the germline and is downregulated around 10 cell diameters from the distal tip (Kocsisova et
907 al., 2019; Shin et al., 2017). Cell diameters were counted from the distal end of the germline up
908 to the row where SYGL-1 is no longer visible by eye. OLLAS staining in the wild-type worms
909 without OLLAS tag was used to differentiate staining from the background. To confirm the
910 accuracy of our visual assessment, we quantified the intensity of SYGL-1 accumulation in the
911 distal germline, employing methods similar to Chen et al., 2020 in the same set of germlines
912 where the SYGL-1 zone was visually evaluated. We found that the cell diameter position called
913 as the end of the SYGL-1 zone consistently corresponded to 6–9% of peak SYGL-1 intensity, for
914 each genotype (Figure 3—figure supplement 2). These results indicate that the SYGL-1 zone
915 length visual assessment was reproducible and consistent.
916
917 Progenitor zone length assessment: The gonads were stained with a progenitor zone marker,
918 anti-CYE-1, and an early meiotic prophase marker, pSUN-1, (anti-SUN-1 S8-Pi) (Mohammad et
919 al., 2018). For assessing the progenitor zone length, cell diameters (rows) were counted from
920 the distal end of the germline, where all cells are CYE-1-positive, until the point after which the
921 majority of the cells in a row have switched from staining for CYE-1 to pSUN-1. Note that pSUN-
922 1 staining is not shown in the figures though it was used to assess the PZ border.
923
924 Assessment of distal position of Sh1: anti-GFP antibody staining was used to visualize the
925 sheath, where cell diameters were counted from distal end to the point where GFP staining
926 became prominent.

927

928 To quantify the distance from the distal end to the border of expression of any protein, we have
929 used either ~30 gonads for single-replicate experiments and ~20 gonads for multi-replicate
930 experiments. We define a biological replicate as independently dissected and stained, along
931 with the controls in the same tube, and images acquired with the same settings. During these
932 experiments, no outliers were encountered. In rare cases, acquired images, which either failed
933 to stitch by Fiji or had poor staining, were discarded.

934

935 Primary antibodies used: mouse anti-CYE-1 (1:100; (Brodigan et al., 2003)); guinea pig anti-SUN-
936 1 S8-Pi (1:1000; (Penkner et al., 2009)); rat anti-OLLAS (1:2000; Novus Biological); rabbit anti-
937 GFP (1:200; from Swathi Arur, MD Anderson Cancer Center; Lopez et al., 2013); and rabbit anti-
938 INX-8 (1:25; Starich et al., 2014)

939

940 Secondary antibodies used: Alexa Fluor 647 goat anti-mouse (Life Technologies, Carlsbad, CA);
941 Alexa Fluor 594 goat anti-guinea pig (Invitrogen, Waltham, MA), Alexa Fluor 594 donkey anti-rat
942 (Invitrogen); and Alexa Fluor 488 goat anti-rabbit (Invitrogen).

943

944

945

946 **Funding**

947 ACS grant PF-19-231-01-CSM to TT

948 NIH R35GM134876 and R01AG065672 to EJAH

949 R01 GM100756 to T. Schedl

950 NIH R01GM57173 and R35GM144029 to DG

951 NIH Office of the Director R24OD010943 to DHH

952

953

954 **Competing interests**

955 E.J.A.H. holds US patent 6,087,153.

956 **Figure Legends**

957

958 **Figure 1.** Germline and somatic gonad innexins are required for proper somatic gonad
959 architecture. A. Schematic of paired somatic and germline octameric hemichannels. B.
960 Schematic diagram of the *inx-8 inx-9* locus and the *inx-14* locus, with relevant mutations
961 indicated in red. C. Fluorescent confocal maximum projection images of distal gonads in live
962 worms. Distal tip cell (DTC) marked in magenta (*naIs37[lag-2p::mCherry-PH]*) and sheath pair 1
963 (Sh1) marked in green (*bcIs39[lim-7p::CED-1::GFP])*. Top: strain bearing markers only, denoted
964 "wild-type", representative of phenotypic Classes 1 and 2. D. *inx-14(ag17)* and *inx-*
965 *8(tn1513tn1555) inx-9(ok1502)*, denoted "*inx-8(rf)*" after Starich et al. (2020), representative of
966 Class 3. E. Diagram of DTC–Sh1 relationship in distal end of a typical wild-type gonad (DTC
967 magenta, Sh1 green) for phenotypic Classes 1–3. Class 1: greater than 8 µm (two cell diameters)
968 separates the proximal most extent of the DTC (vertical line topped with magenta dot) and the
969 distal most border of Sh1 (vertical line topped with green dot) as measured in slice-by-slice
970 analysis of Z series; Class 2: ≤8 µm separates DTC and Sh1 extensions or interdigitation of DTC
971 and Sh1 is seen up to the position of the average DTC process length (vertical line topped with
972 blue dot); Class 3: distal position of Sh1 is distal to the average DTC process length. A diagram of
973 all measurements taken for live fluorescent images is shown in Figure 1—figure supplement 1.
974 F. The proportion of gonads examined that fall into the phenotypic classes indicated. G. Plot
975 showing the distance between the average DTC process length (blue dots), the longest DTC
976 process (magenta dots) and the distal-most border of Sh1 (green dots); each trio of dots joined
977 by a dark blue line represents the data for a single gonad, analyzed as a confocal maximum
978 projection. Scale bars are 10 µm. Strains used are DG5020, DG5026 and DG5029. See
979 Supplementary File 1 for complete genotypes.

980

981

982 **Video 1.** Confocal stack and 3D rendering of representative Class 1 gonad. Strain DG5020.
983 **Video 2.** Confocal stack and 3D rendering of representative Class 2 gonad. Strain DG5020.
984 **Video 3.** Confocal stack and 3D rendering of representative Class 3 gonad. Strain DG5026.

985

986

987 **Figure 1—figure supplement 1.** Consistent trends in Sh1 and DTC positions are observed with
988 multiple markers.
989 A. Schematic diagram of DTC and Sh1 parameters measured. Each black dot represents a point
990 in a maximum projection Z-stack for which the distance from the distal end was measured in
991 microns. B. Fluorescent micrographs of gonads in live worms bearing indicated markers that
992 label DTC (magenta lettering) or Sh1 (green lettering), in wild-type and *inx-14(ag17)* mutant
993 backgrounds, as indicated: *naIs37*, *bcIs39*, *qIs154*, and *tnIs5* are integrated transgenes; *tnEx42*
994 carries a rescuing *acy-4p*::*gfp* fusion on an extrachromosomal array; and *fasn-1(av138[fasn-*
995 *1::gfp])* was tagged at the endogenous locus using CRISPR-Cas9 genome editing (see
996 Supplementary File 1 for full genotypes). The *fasn-1* and *acy-4* fusions also drive expression in
997 non-gonadal tissues. C. The proportion of gonads examined that fall into the phenotypic classes
998 indicated. D. Plot showing the distance between the average DTC process length (blue dots),
999 the longest DTC process (magenta dots) and the distal-most border of Sh1 (green dots); each
1000 trio of dots joined by a dark blue line represents the data for a single gonad. E. Plots showing
1001 quantitative measurement of parameters diagrammed in (A). Although the behavior of the
1002 DTCs marked by different markers is variable, and DTCs marked with *qIs154* show significantly
1003 longer DTC processes, the behavior of Sh1 in the presence of either marker shows significantly
1004 consistent changes across mutant genotypes. All *P* values result from Student's *t*-test. Scale
1005 bars are 10 µm. Strains used were DG5020, DG4959, DG4977, DG5026, DG5320, DG5367,
1006 DG5310. See Supplementary File 1 for complete genotypes.

1007

1008

1009 **Figure 1—figure supplement 2.** Snapshot of transmission electron micrograph (TEM)
1010 reconstruction and guide to Videos 4 and 5.

1011

1012 **Video 4.** Serial thin section movie of every third section from the DTC to the distal extensions of
1013 Sh1 in a young adult hermaphrodite posterior gonad arm. Germ cell nuclei are marked in yellow

1014 if the corresponding germ cells receive direct contact from a DTC or Sh1 process, or in salmon if
1015 they do not. The soma and processes of the DTC are filled in pink. Filopodial extensions of the
1016 somatic sheath are filled in green. Individual images are composed from multi-panel montages
1017 (mostly 3 x 4 montages). Scale bar is 3 µm. Video 4 is available at
1018 https://datadryad.org/stash/share/CgAYZh4cDADyskEuMQwsWj_3f93PSl9_ETgna-uVRYI
1019 or at https://s3.msi.umn.edu/greenste/Video4_R1.avi
1020
1021 **Video 5.** Model of the distal gonad. The DTC, its processes and fragments are in pink. Nearest
1022 sheath cell bodies lie out of frame proximally, but their filopodial extensions are shown in
1023 green, extending towards the DTC. Germ cell nuclei are modelled as spheres; the nuclei of
1024 those germ cells that do not come in contact with either DTC or Sh1 are colored in salmon,
1025 while germ cells with direct contact are shown in yellow. The true volume of each germ cell is
1026 larger than is shown here because each sphere is centered only on the cell nucleus. Scale bar is
1027 5 µm.
1028
1029
1030 **Figure 2.** N-terminal fusion of mKate2 to INX-8 generates an INX-8 protein that alters somatic
1031 gonad morphology. A. Schematic diagram showing the genetic manipulations used in this
1032 section. *inx-8(qy78[mKate2::inx-8])* was created by placing mKate2 in-frame with the N-
1033 terminus of INX-8 (Gordon et al., 2020). *inx-8(qy78tn2031)* was created by deleting the *inx-8*
1034 coding region and mKate2 moiety in the *inx-8(qy78)* background. B. Representative distal
1035 gonads stained with anti-INX-8 antibody; Top: N2 wild-type, Bottom: DG5063 *inx-*
1036 *8(qy78[mKate2::inx-8]).* C. Dot plot with overlaid quantile box plots showing the distance from
1037 the distal end of the gonad to the Sh1 distal border for each genotype. Each dot represents a
1038 single gonad of that genotype. *P* value was calculated using Student's *t*-test. D. Fluorescent
1039 micrographs of live animals with the DTC marked by *naIs37[lag-2p::mCherry-PH]* and Sh1
1040 marked by *bcIs39[lim-7p::ced-1::gfp]*. Top: wild-type with markers only. Middle: *inx-*
1041 *8(qy78[mKate2::inx-8])*. Bottom: *inx-8(qy78tn2031).* E. Quantitative dot-plots as in Figure 1;
1042 data for wild-type (marker only) strain in E is the same as in Figure 1. Each pair of dots

1043 connected by a line represents data from a single gonad. Scale bar 10µm. Strains used were N2,
1044 DG5063, DG5020, DG5131, DG5229, DG5320, DG5378. See Supplementary File 1 for complete
1045 genotypes.
1046
1047 **Figure 2—figure supplement 1.** Detection of INX-8 antibody overlaps with mKate2 fluorescence
1048 in *inx-8(qy78[mKate2::inx-8)]*. Representative image of dissected distal gonad stained with
1049 anti-INX-8 antibody (top, green), mKate2 fluorescence (middle, red) and merged (bottom,
1050 yellow) in DG5063 *inx-8(qy78[mKate2::INX-8])*. The distal end of the gonad is on the left. In all
1051 gonads examined (n=32), overlap was complete. Scale bars are 10 µm.
1052
1053 **Figure 2—figure supplement 2.** The *inx-8(qy78[mKate2::inx-8)* allele behaves as a dosage-
1054 sensitive antimorph. A. Schematic diagram showing additional relevant alleles at the *inx-8* and
1055 *inx-9* loci. B–E. Relevant genotypes are given for *inx-8* and *inx-9* only. All strains also contain
1056 *naIs37* to mark the DTC and *bcIs39* to mark Sh1. *inx-8(qy78[mKate2::inx-8])* and *inx-*
1057 *8(qy102[mKate2::inx-8])* are abbreviated as *inx-8(qy78)* and *inx-8(qy102)* to aid comparisons
1058 between genotypes. B. Representative fluorescent micrographs of live worms carrying each
1059 relevant allele, as indicated (images for *inx-8(+), inx-8(qy78[mKate2::inx-8])* and *inx-*
1060 *8(qy102tn2031)* are the same as in Fig. 2B, included here for comparison). C. Stacked histogram
1061 showing the frequency of each of the phenotypic classes described in Fig. 1, for each genotype,
1062 as indicated. D. Table showing frequency of Class 3 gonads for each genotype, with indicated
1063 pairwise significance levels derived from a Fisher's Exact Test. E. Quantitative plots showing
1064 changes to DTC morphology and Sh1 position. All *P* values result from Student's *t*-test. Scale
1065 bars are 10 µm. Strains used were DG5020, DG5131, DG5229, DG5232, DG5027, DG5133,
1066 DG5346, DG5347, DG5366. See Supplementary File 1 for complete genotypes.
1067
1068 **Figure 2—figure supplement 3.** Direct comparison of *inx-8(qy78[mKate2::inx-8]* and *lim-7p-*
1069 driven transgenes as markers for Sh1. A. Individual gonads carrying different Sh1 markers in
1070 addition to *inx-8(qy78[mKate2::inx-8]).* Left, top to bottom: Individual channels and merged
1071 image of a single worm co-expressing the DTC marker *cpIs122[lag-2p::gfp], inx-*

1072 *8(qy78[mKate2::inx-8])* and the sheath cell marker *tnIs5[lim-7p::gfp]*. Right, top to bottom:
1073 Individual channels and merged image of a single worm co-expressing the DTC marker
1074 *naIs37[lag-2p::mCherry-PH]*, *inx-8(qy78[mKate2::inx-8])* and the sheath cell marker *bcIs39[lim-*
1075 *7p::ced-1::gfp]*. B. Two individual gonads of the same genotypes as in (A), showing incomplete
1076 overlap between mKate2::INX-8 and the respective GFP sheath cell markers. White arrowheads
1077 mark the most distal extent of each marker in the single-channel panels. C and D: *inx-*
1078 *8(qy78[mKate2::inx-8]* is abbreviated as "*inx-8(qy78)".* C. Frequency of overlap. Of 46 gonads
1079 examined, 39 showed perfect overlap as shown in these images. D. Proportion of gonads in
1080 phenotypic Classes 1–3 as scored by mKate2 or as scored by GFP expression, as indicated by
1081 bold in the genotype. Scale bars are 10 µm. Strains used were DG5020, DG5131, KLG006. See
1082 Supplementary File 1 for complete genotypes.
1083
1084
1085 **Figure 3**. The position of the proximal border of the SYGL-1-positive stem cell pool does not
1086 correlate with the position of Sh1. A. Fluorescence confocal maximum projection of surface
1087 images (~7 µm depth) of fixed, dissected gonads showing the SYGL-1-positive stem cell pool
1088 marked in magenta and the sheath cell marked in green. Magenta caret represents the location
1089 of the proximal border of the SYGL-1-positive stem cell pool. Green caret represents the distal
1090 edge of Sh1. B. Quantitative graph with magenta dots representing the proximal border of
1091 SYGL-1::OLLAS expression and green dots representing the distal reach of Sh1. Each pair of dots
1092 connected by a line represents the data for a single gonad. C. Dot plot with overlaid box plots
1093 showing the distance and quantiles of the SYGL-1-positive stem cell pool and distal extent of
1094 Sh1 for each genotype. Each dot represents a single specimen of that genotype. *P* values were
1095 calculated using Student's *t*-test. D. Scatterplot showing lack of correlation between the
1096 proximal extent of SYGL-1 expression and the distal reach of Sh1. Scale bars are 10 µm. Strains
1097 used are DG5136, DG5150, DG5181, DG5248, and DG5249. See Supplementary File 1 for
1098 complete genotypes.
1099

1100 **Figure 3—figure supplement 1.** The position of the proximal border of the SYGL-1-positive
1101 stem cell pool does not correlate with the position of Sh1 when data are shown in cell
1102 diameters. A. Quantitative graph with magenta dots representing the proximal extent of SYGL-
1103 1::OLLAS expression and green dots representing the distal reach of Sh1. Each pair of magenta
1104 and green dots connected by a line represents the data for a single gonad. B. Dot plot with
1105 overlaid box plots showing the distance and quantiles of the SYGL-1-positive stem cell pool and
1106 distal extent of Sh1 for each genotype, in cell diameters from the distal end. Each dot
1107 represents a single specimen of that genotype. *P* values were calculated using Student's *t*-test.
1108 C. Scatterplot showing lack of correlation between the proximal extent of SYGL-1 expression
1109 and the distal reach of Sh1. CD: cell diameters. Strains used are listed in Figure 3.
1110
1111 **Figure 3—figure supplement 2.** Proximal end of the SYGL-1 zone assessed visually and from
1112 protein levels. SYGL-1 (3xOLLAS::SYGL-1) levels were measured from the distal tip of the gonad
1113 to (A) 25 CD and (B) 100 microns proximal, in dissected and stained gonads from 1-day adults
1114 of the indicated genotypes. The visually assessed SYGL-1 border and the distal extent of Sh1
1115 are marked. SYGL-1 protein levels from fluorescence-intensity measurements are normalized
1116 by setting the peak levels in wild type to 100. The SYGL-1 quantitation of the indicated
1117 genotype is carried out for the gonads in Fig. 3B. The small differences observed in SYGL-1 peak
1118 levels between wild type and *inx-14(ag17)* or *inx-8(qy78[mKate2::inx-8])* are not statistically
1119 significant (Student's *t*-test). Triangle, distal most position (start) of Sh1; circle, proximal
1120 position of SYGL-1 staining; blue, wild type; red *inx-14(ag17)*; black *inx-8(qy78[mKate2::inx-8])*.
1121 Curved plot lines, mean; vertical bars, mean ± SD. All three strains have *sygl-1(q983) naIs37 I;*
1122 *bcIs39 V* in the background along with the indicate *inx-x* genotype. Strains used are DG5136,
1123 DG5150, and DG5181. See Supplementary File 1 for complete genotypes.
1124
1125
1126 **Figure 4.** The position of the proximal border of the progenitor zone does not correlate with the
1127 position of Sh1. A. Fluorescence confocal maximum projection of surface images (~7 µm depth)
1128 of fixed, dissected gonads showing the progenitor pool marked in magenta and the sheath cell

1129 marked in green. All measurements were made by examining optical sections through the
1130 entire depth of the gonad. Magenta caret represents the location of the proximal border of the
1131 CYE-1-positive, pSUN-1-negative progenitor pool (pSUN-1 staining not shown; see Materials
1132 and Methods). Green caret represents the distal edge of Sh1. B. Quantitative graph with
1133 magenta dots representing the proximal extent of the CYE-1 staining and green dots
1134 representing the distal reach of Sh1. Each pair of magenta and green dots connected by a line
1135 represents the data for a single gonad. C. Dot plot with overlaid box plots showing the distance
1136 and quantiles of the progenitor pool and distal extent of Sh1 for each genotype. Each dot
1137 represents a single specimen of that genotype. *P* values were calculated using Student's *t*-test.
1138 D. Scatterplot showing lack of correlation between the proximal PZ border and Sh1 position.
1139 Scale bars are 10 µm. Strains used are DG5136, DG5150, DG5181, DG5248, and DG5249. See
1140 Supplementary File 1 for complete genotypes.
1141
1142 **Figure 4–figure supplement 1.** The position of the proximal border of the progenitor zone does
1143 not correlate with the position of Sh1 when data are shown in cell diameters. A. Quantitative
1144 graph with magenta dots representing the location of the proximal border of the CYE-1-
1145 positive, pSUN-1-negative progenitor pool and green dots representing the proximal extent of
1146 and green dots representing the distal reach of Sh1. Each pair of magenta and green dots
1147 connected by a line represents the data for a single gonad. B. Dot plot with overlaid box plots
1148 showing the distance and quantiles of the CYE-1-positive progenitor pool and distal extent of
1149 Sh1 for each genotype, in cell diameters from the distal end. Each dot represents a single
1150 specimen of that genotype. *P* values were calculated using Student's *t*-test. C. Scatterplot
1151 showing lack of correlation between the proximal extent of progenitor zone and the distal
1152 reach of Sh1. CD: cell diameters. Strains used are listed in Figure 4.
1153
1154 **Figure 5.** Reduced innexin function shifts Sh1 distally, eliminating the bare regions between the
1155 DTC and Sh1, but this shift does not alter the border of the stem cell pool.
1156
1157 **Supplementary File 1.** Strains used in this study.

1158

1159 **Supplementary File 2.** Oligonucleotides used in this study.

1160

1161 **Table 1—Source data 1.** Brood size and embryonic lethality data for Table 1.

1162 **Figure 1—Source data 1.** Source data for Figure 1C–D and Figure 1F–G

1163 **Figure 1—figure supplement 1—Source data 1.** Source data for Figure 1—figure supplement 1

1164 panels B–E.

1165 **Figure 2—Source data 1.** Source data for Figure 2B and C

1166 **Figure 2—Source data 2.** Source data for Figure 2D–F.

1167 **Figure 2—figure supplement 2—Source data 1.** Source data for Figure 2—figure supplement 2

1168 panels B–E.

1169 **Figure 2—figure supplement 3—Source data 1.** Source data for Figure 2—figure supplement 3.

1170 **Figure 3—Source data 1.** Source data for Figure 3 and Figure 3—figure supplement 1.

1171 **Figure 4—Source data 1.** Source data for Figure 4 and Figure 4—figure supplement 1.

1172

1173

Figure 1

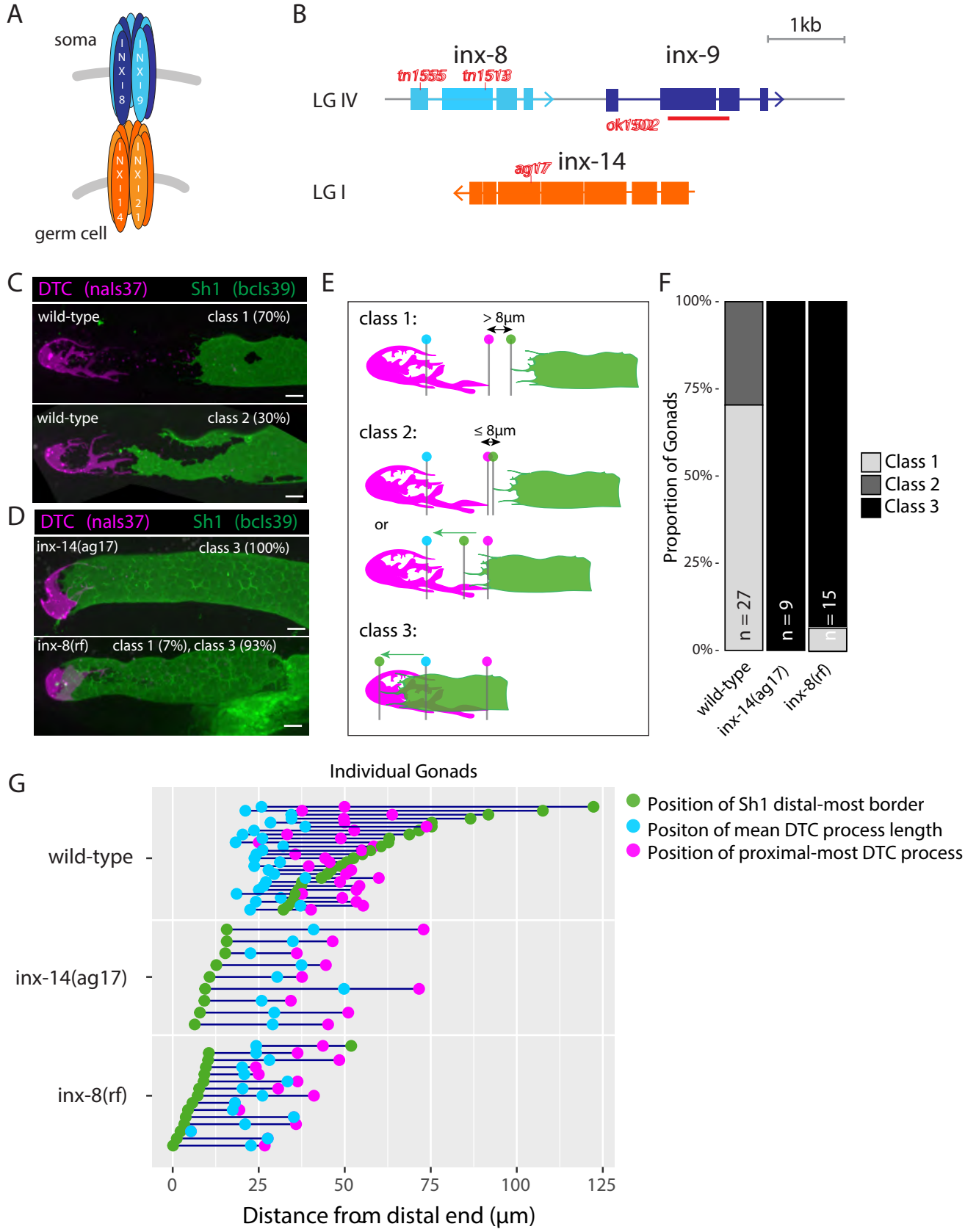
A
soma
germ cell
INX8
INX9
INX14
INX21
B
1kb
inx-8
inx-9
tn1555
tn1513
LG IV
ok1502
ag17
inx-14
LG I
C
DTC (nals37)
Sh1 (bcls39)
wild-type
class 1 (70%)
wild-type
class 2 (30%)
D
DTC (nals37)
Sh1 (bcls39)
inx-14(ag17)
class 3 (100%)
inx-8(rf)
class 1 (7%), class 3 (93%)
E
class 1:
> 8µm
class 2:
≤ 8µm
or
class 3:
F
100%
75%
50%
25%
0%
Proportion of Gonads
n = 27
n = 9
n = 15
wild-type
inx-14(ag17)
inx-8(rf)
Class 1
Class 2
Class 3
G
Individual Gonads
wild-type
inx-14(ag17)
inx-8(rf)
0
25
50
75
100
125
Distance from distal end (µm)
Position of Sh1 distal-most border
Positon of mean DTC process length
Position of proximal-most DTC process

Figure 1—figure supplement 1

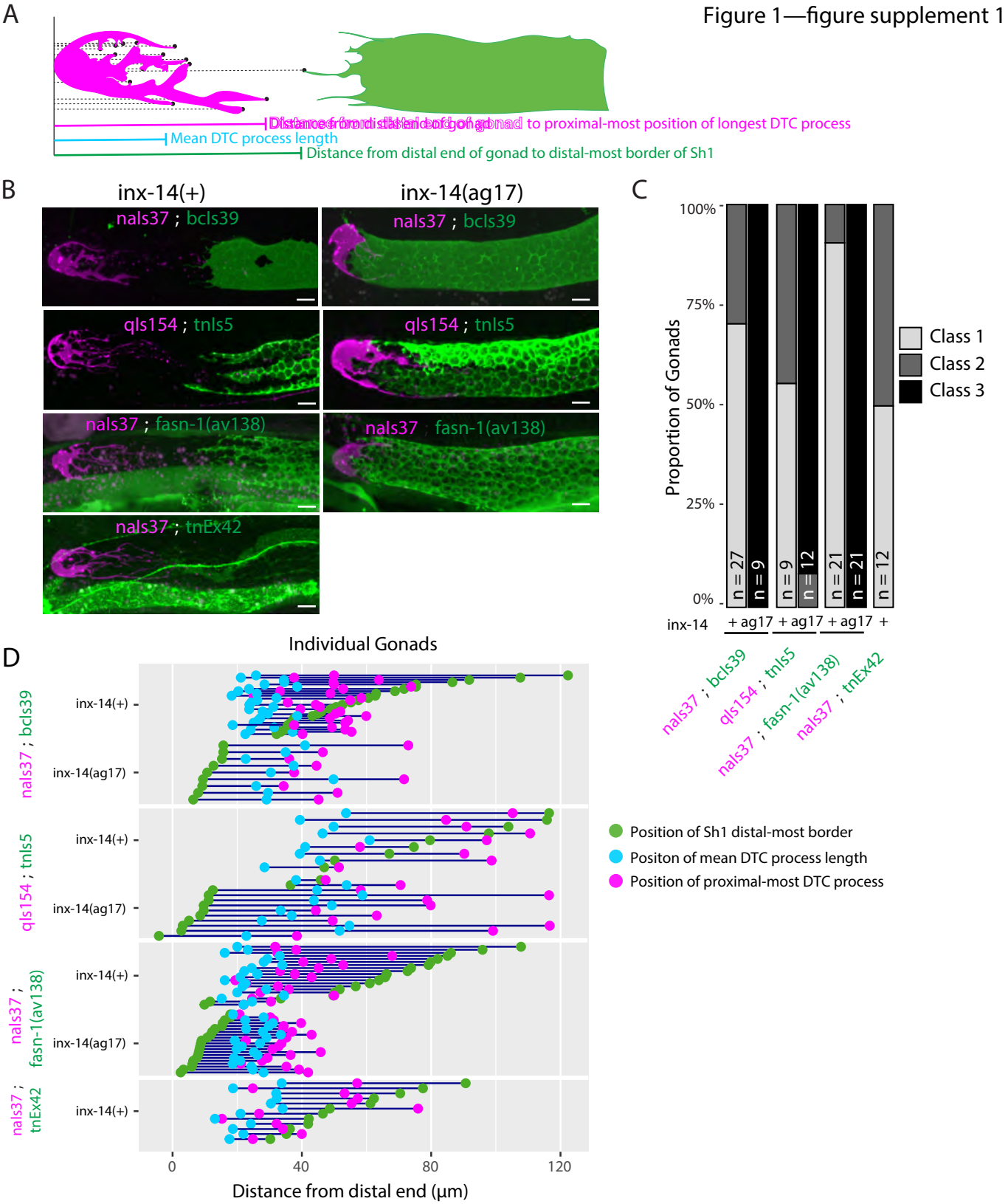

Figure 1—figure supplement 2

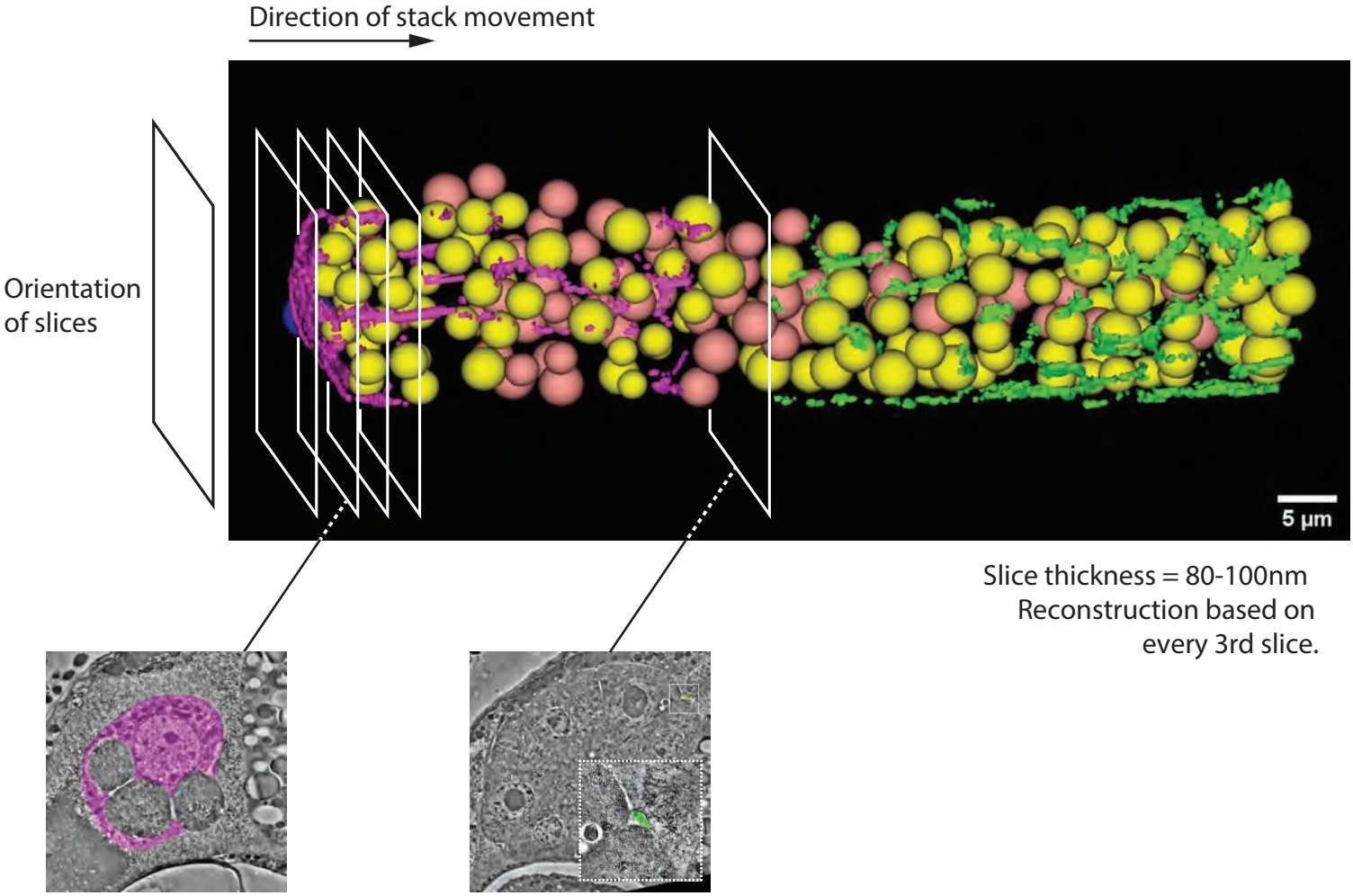

Figure 2

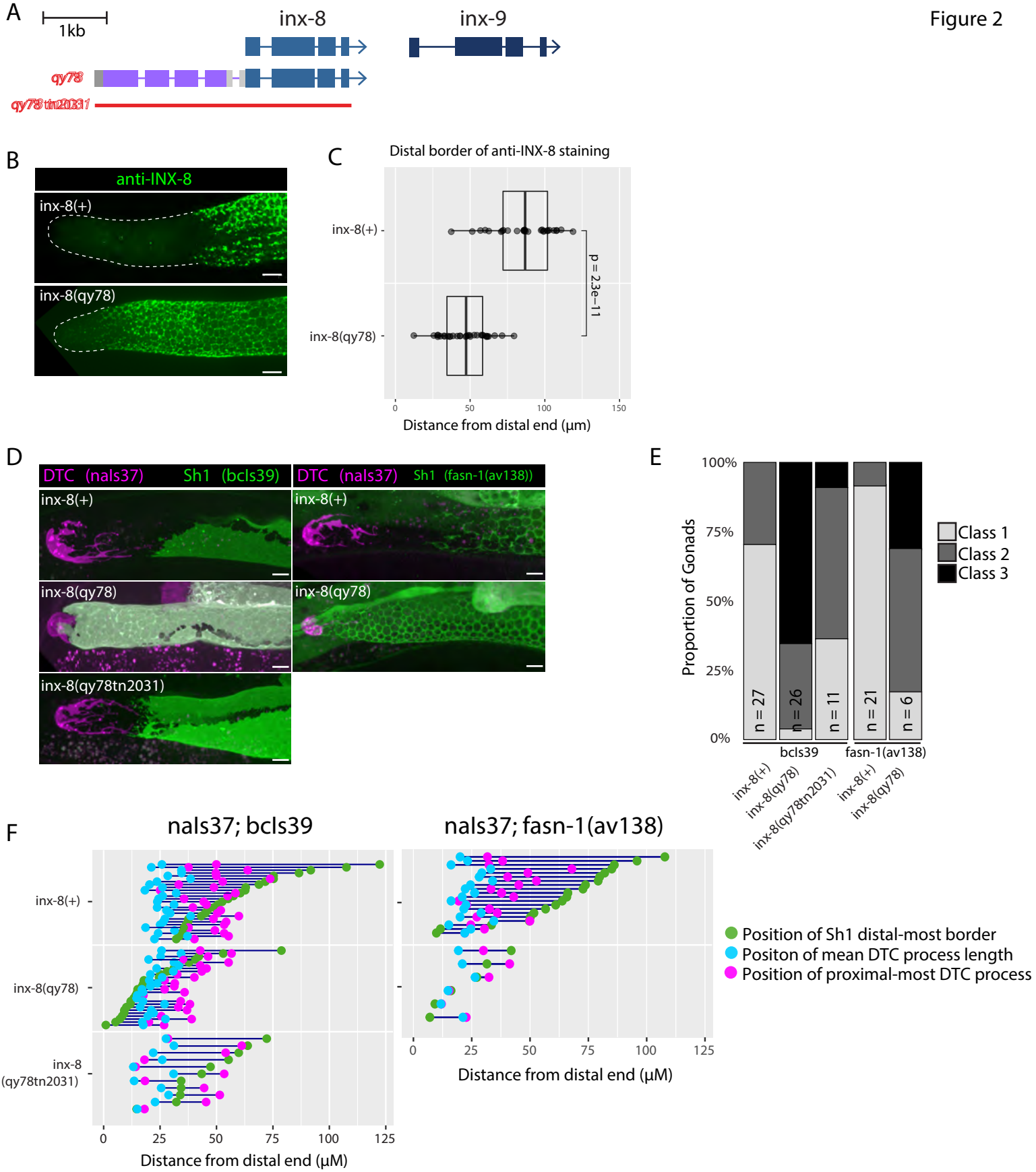
A
1kb
inx-8
inx-9
qy78
qy78 tn2031
B
anti-INX-8
inx-8(+)
inx-8(qy78)
C
Distal border of anti-INX-8 staining
inx-8(+)
inx-8(qy78)
p = 2.3e−11
0
50
100
150
Distance from distal end (µm)
D
DTC (nals37) Sh1 (bcIs39)
DTC (nals37) Sh1 (fasn-1(av138))
inx-8(+)
inx-8(qy78)
inx-8(qy78tn2031)
E
Proportion of Gonads
100%
75%
50%
25%
0%
n = 27
n = 26
n = 11
n = 21
n = 6
bcIs39
fasn-1(av138)
inx-8(+)
inx-8(qy78)
inx-8(qy78tn2031)
Class 1
Class 2
Class 3
F
nals37; bcIs39
nals37; fasn-1(av138)
inx-8(+)
inx-8(qy78)
inx-8 (qy78tn2031)
0
25
50
75
100
125
Distance from distal end (µM)
Position of Sh1 distal-most border
Positon of mean DTC process length
Position of proximal-most DTC process

Figure 2—figure supplement 1

DG5063(inx-8(qy78[mKate::inx-8])

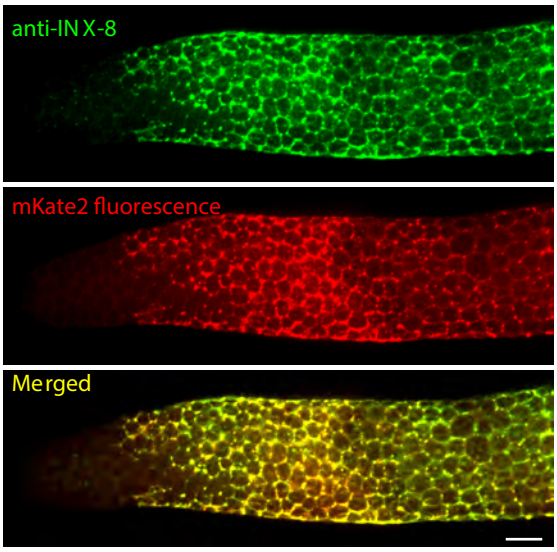

Figure 2—figure supplement 2

A

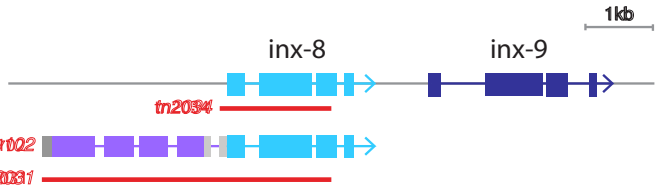

B

All panels: DTC marked with nals37 and Sh1 with bcIs39

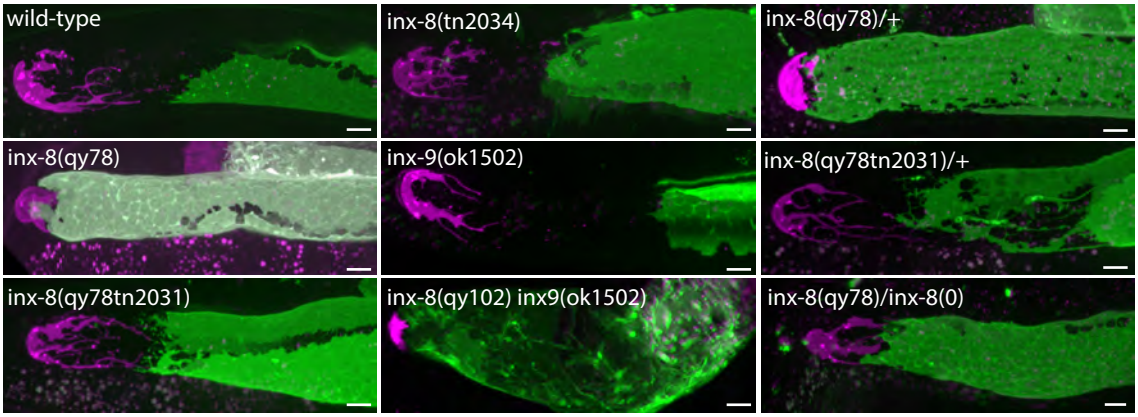

C

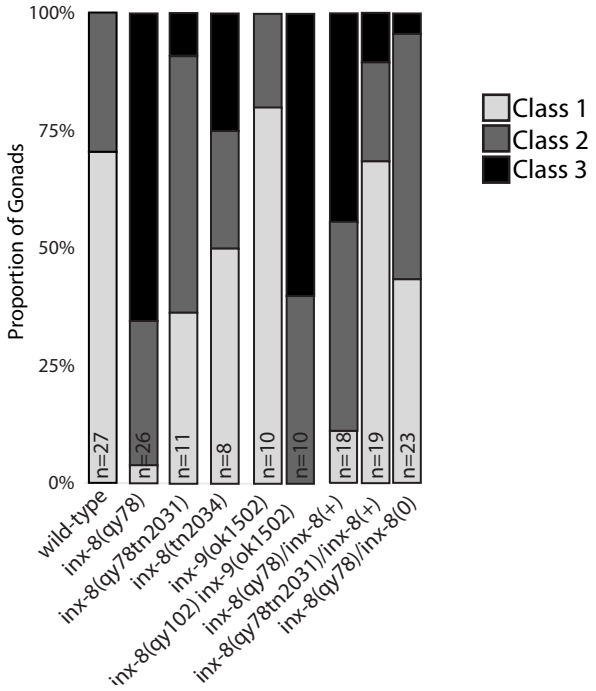

D

Relevant Genotype	%Class 3	p-value
inx-8(+) inx-9(+)	0%	
inx-8(qy78)	65%	
inx-8(qy78tn2031)	9%	
inx-8(tn2034)	25%	
inx-9(ok1502)	0%	
inx-8(qy102) inx-9(ok1502)	60%	
inx-8(qy78)/inx-8(+)	44%	
inx-8(qy78tn2031)/inx-8(+)	10%	
inx-8(qy78)/inx-8(0)	4%	

*P ≤ 0.01 ** P ≤ 0.001 ***P ≤ 0.0001

E

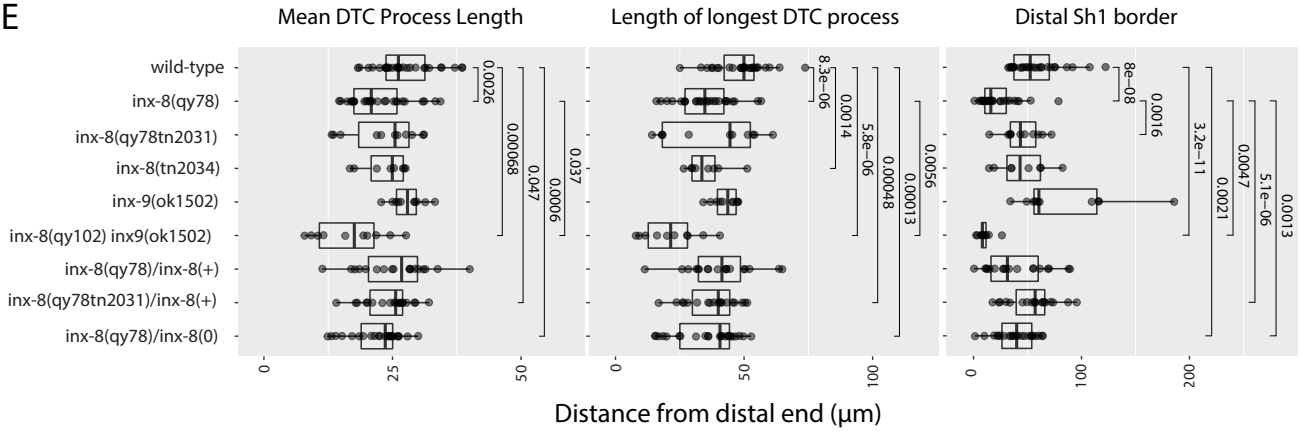

A Complete overlap > 80%

cpIs122[lag-2p::GFP];
inx-8(qy78[mKate2::inx-8]);
tnIs5[lim-7p::GFP]

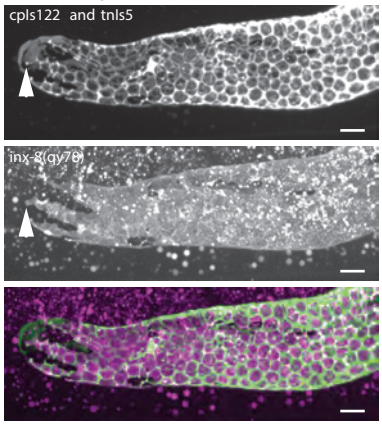

naIs37[lag-2p::mCherry];
inx-8(qy78[mKate2::inx-8]);
bcIs39[lim-7p::ced-1::gfp]

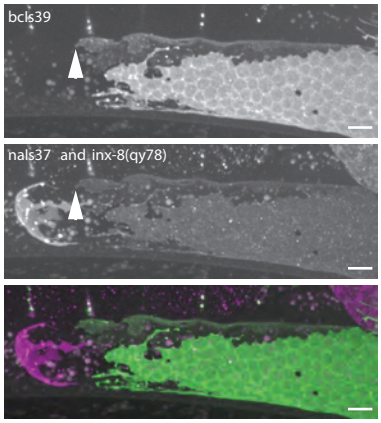

B Incomplete overlap < 20%

cpIs122[lag-2p::GFP];
inx-8(qy78[mKate2::inx-8]);
tnIs5[lim-7p::gfp]

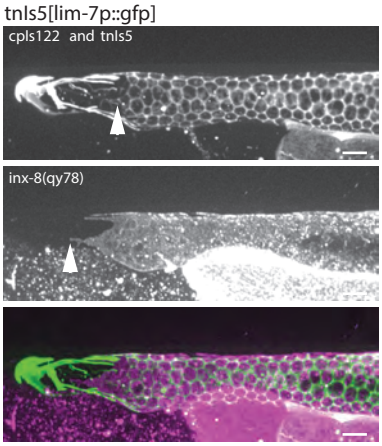

naIs37[lag-2p::mCherry];
inx-8(qy78[mKate2::inx-8]);
bcIs39[lim-7p::ced-1::gfp]

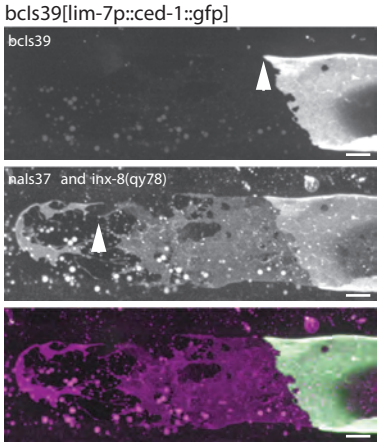

C

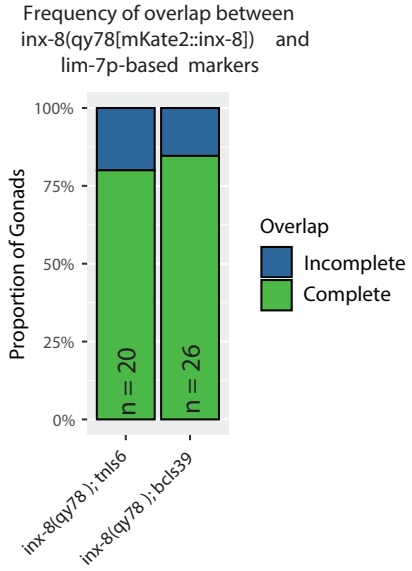

D

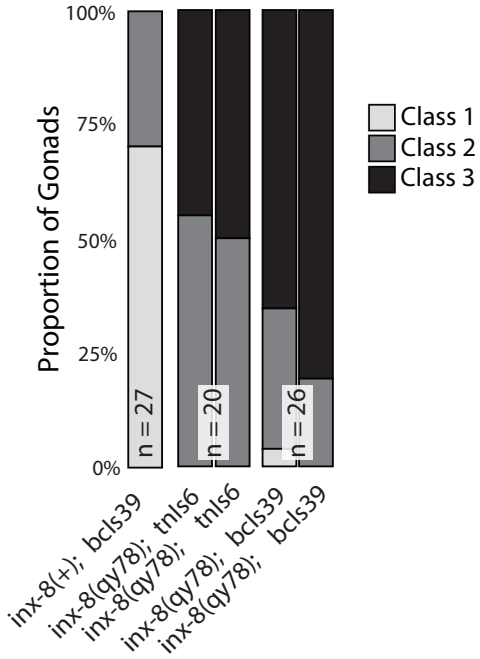

Figure 3

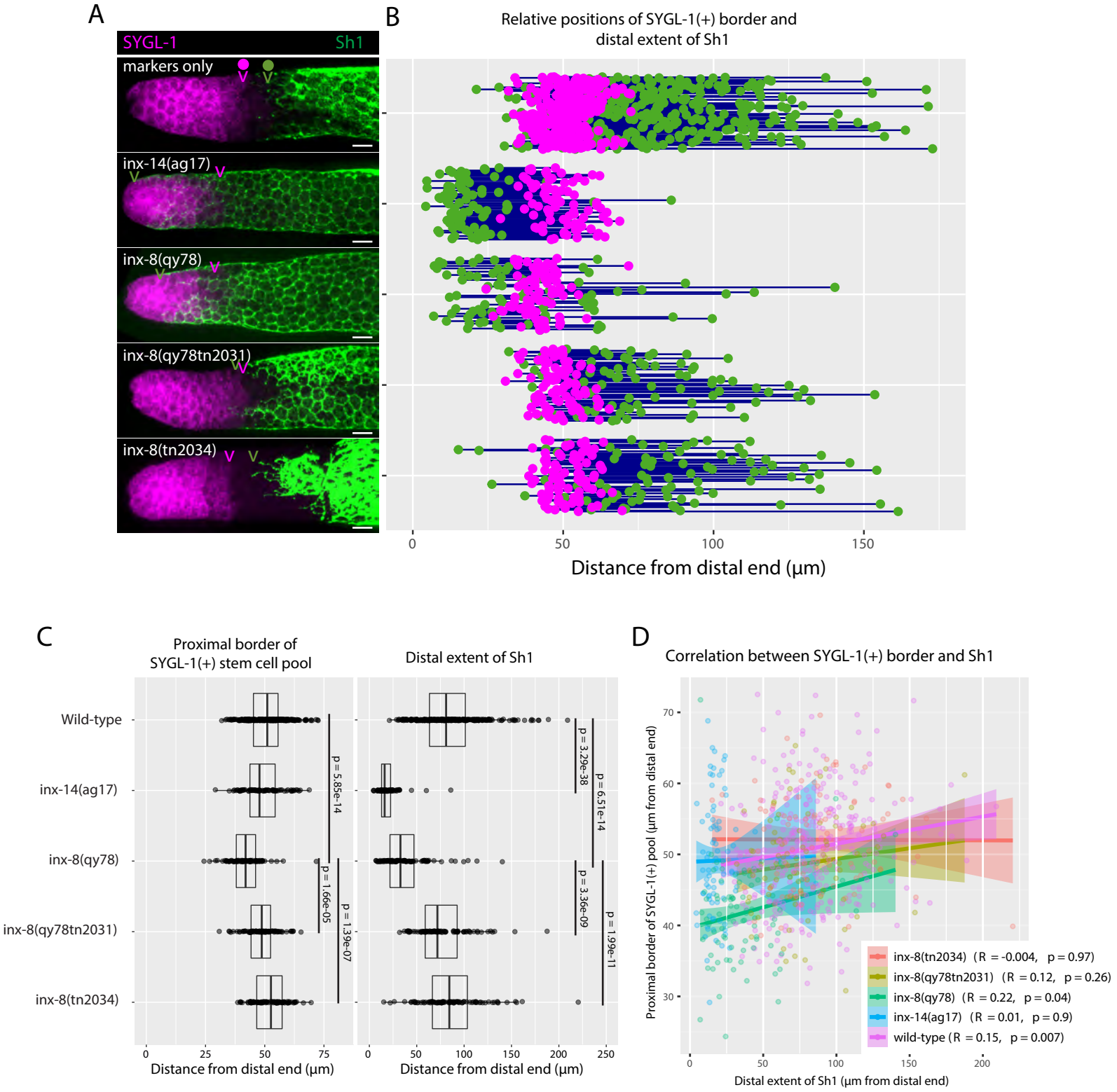
A
SYGL-1
Sh1
markers only
inx-14(ag17)
inx-8(qy78)
inx-8(qy78tn2031)
inx-8(tn2034)
B
Relative positions of SYGL-1(+) border and distal extent of Sh1
0
50
100
150
Distance from distal end (µm)
C
Proximal border of SYGL-1(+) stem cell pool
Distal extent of Sh1
Wild-type
inx-14(ag17)
inx-8(qy78)
inx-8(qy78tn2031)
inx-8(tn2034)
p = 5.85e-14
p = 1.66e-05
p = 1.39e-07
p = 3.29e-38
p = 6.51e-14
p = 3.36e-09
p = 1.99e-11
0
25
50
75
100
150
200
250
Distance from distal end (µm)
D
Correlation between SYGL-1(+) border and Sh1
Proximal border of SYGL-1(+) pool (µm from distal end)
Distal extent of Sh1 (µm from distal end)
inx-8(tn2034) (R = -0.004, p = 0.97)
inx-8(qy78tn2031) (R = 0.12, p = 0.26)
inx-8(qy78) (R = 0.22, p = 0.04)
inx-14(ag17) (R = 0.01, p = 0.9)
wild-type (R = 0.15, p = 0.007)

Figure 3—figure supplement 1

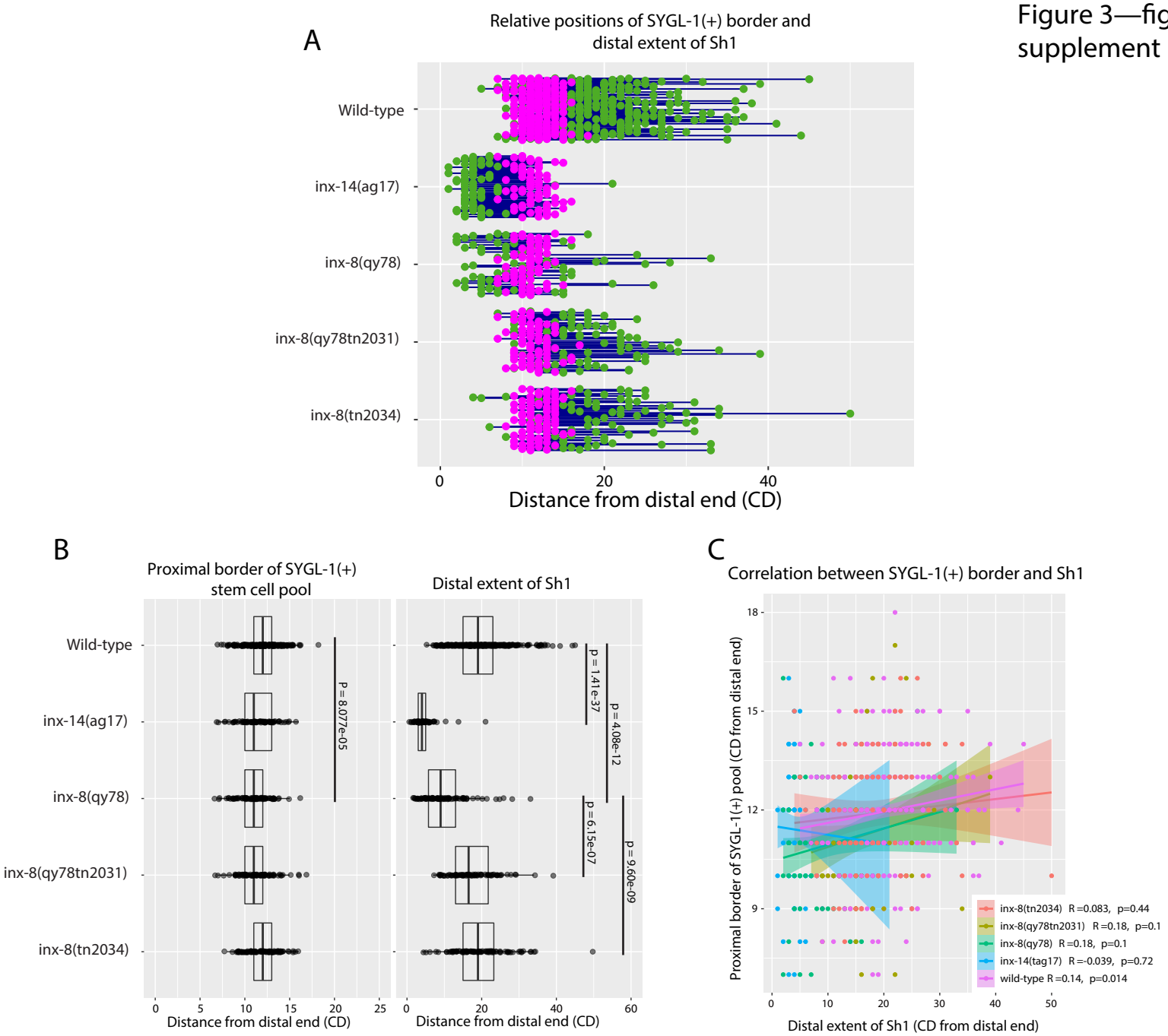

Figure 3—figure supplement 2

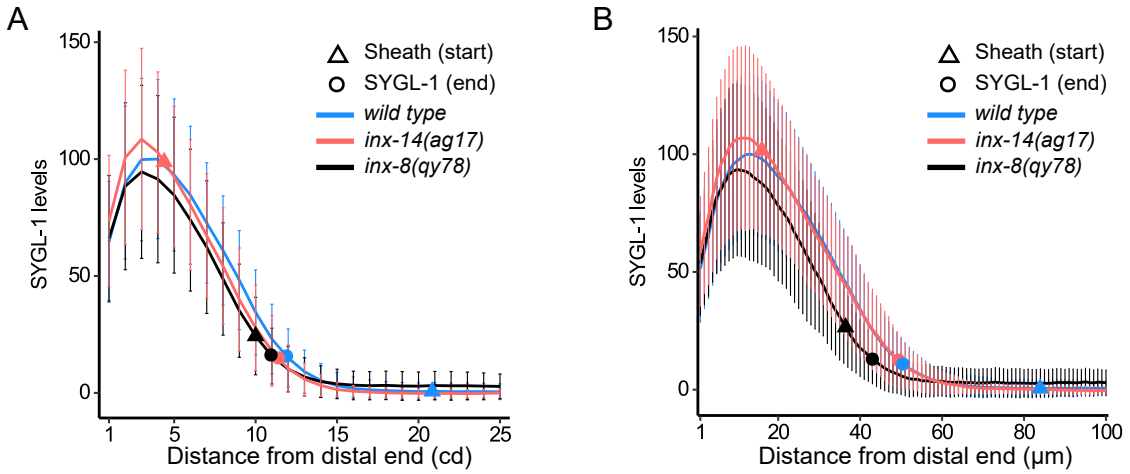

Figure 4

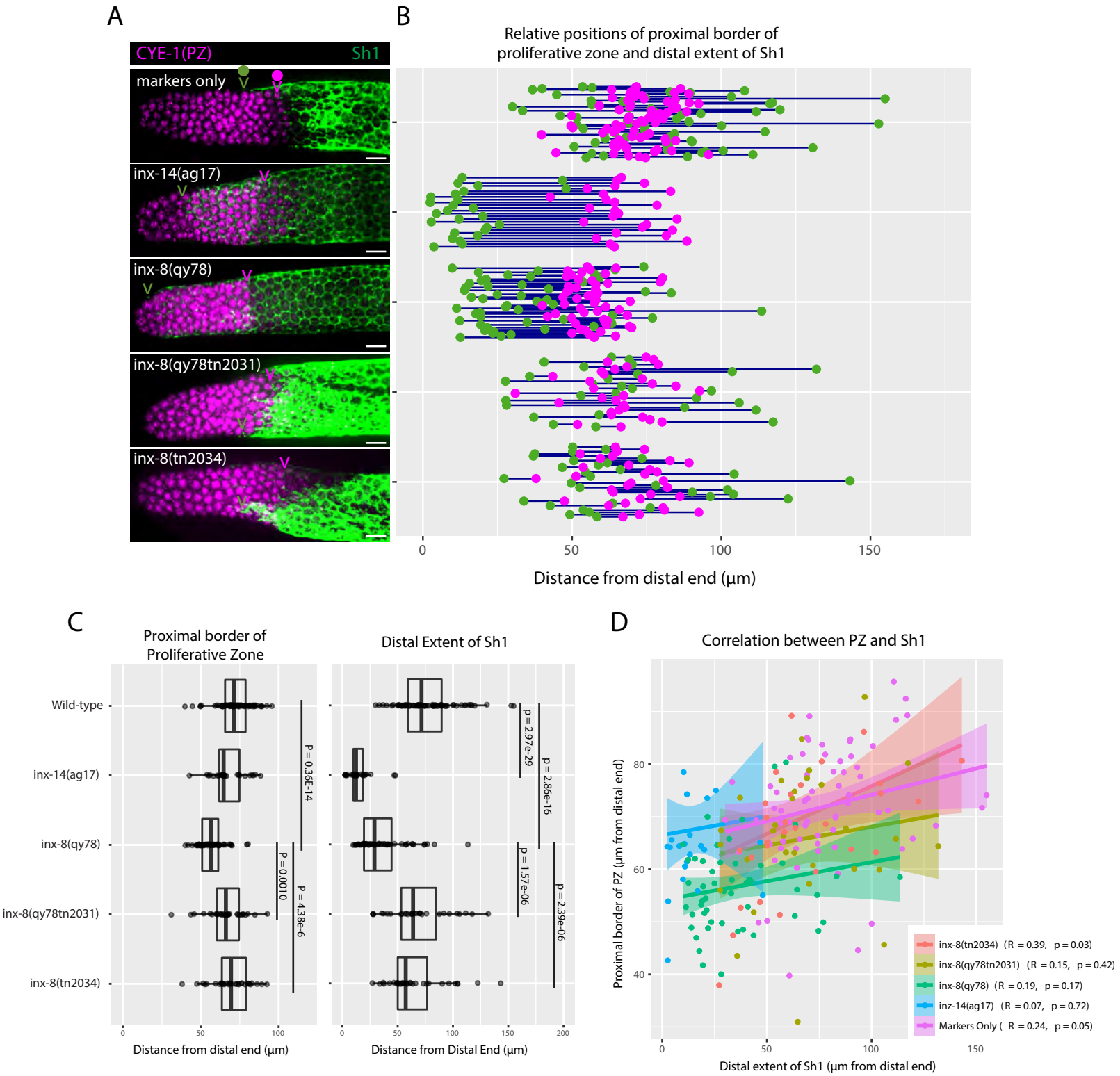
A
CYE-1(PZ)
Sh1
markers only
inx-14(ag17)
inx-8(qy78)
inx-8(qy78tn2031)
inx-8(tn2034)
B
Relative positions of proximal border of proliferative zone and distal extent of Sh1
0
50
100
150
Distance from distal end (µm)
C
Proximal border of Proliferative Zone
Distal Extent of Sh1
Wild-type
inx-14(ag17)
inx-8(qy78)
inx-8(qy78tn2031)
inx-8(tn2034)
P = 0.36E-14
P = 0.0010
P = 4.38e-6
p = 2.97e-29
p = 2.86e-16
p = 1.57e-06
p = 2.39e-06
Distance from distal end (µm)
Distance from Distal End (µm)
D
Correlation between PZ and Sh1
Proximal border of PZ (µm from distal end)
Distal extent of Sh1 (µm from distal end)
inx-8(tn2034) (R = 0.39, p = 0.03)
inx-8(qy78tn2031) (R = 0.15, p = 0.42)
inx-8(qy78) (R = 0.19, p = 0.17)
inz-14(ag17) (R = 0.07, p = 0.72)
Markers Only (R = 0.24, p = 0.05)

Figure 4–figure supplement 1

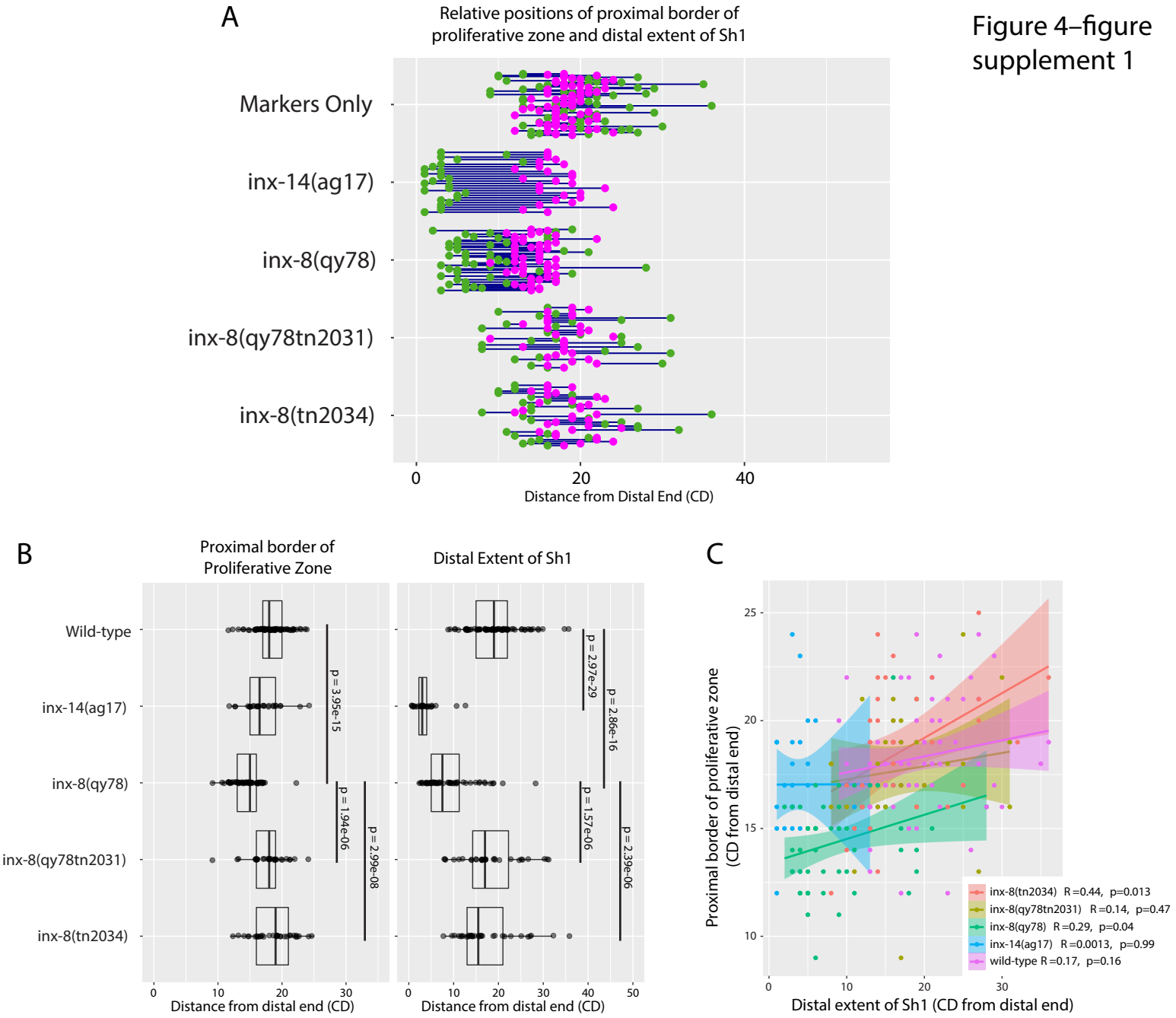

Figure 5

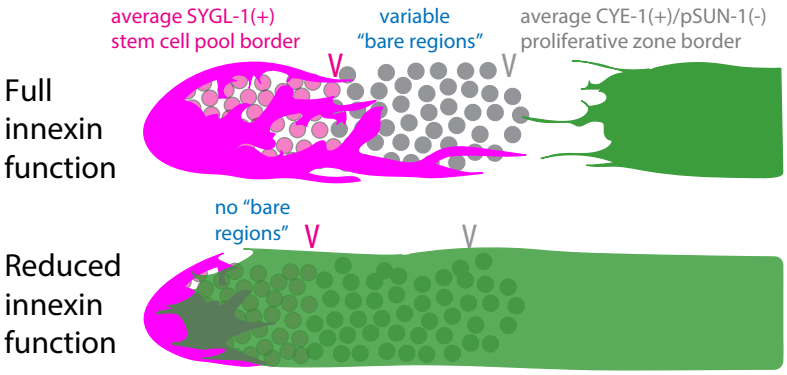
average SYGL-1(+)
stem cell pool border
variable
"bare regions"
average CYE-1(+)/pSUN-1(-)
proliferative zone border
Full
innexin
function
no "bare
regions"
Reduced
innexin
function

Reagent type (species) or resource	Designation	Source or reference	Identifiers	Additional information
Antibody	mouse monoclonal anti-CYE-1	Brodigan et al., 2003		(1:100)
Antibody	rat monoclonal anti-OLLAS	Shin et al., 2017		(1:2000)
Antibody	guinea pig polyclonal anti-SUN-1 S8-Pi	Mohammad et al., 2018		(1:1000)
Antibody	rabbit polyclonal anti-GFP	from Swathi Arur, MD Anderson Cancer Center; Lopez et al., 2013		(1:200)
Antibody	rabbit polyclonal anti-INX-8	Starich et al., 2014		(1:25)
sequence-based reagent	AF-ZF-827	Arribere et al., 2014		CACTTGAACTTCAATA CGGCAAGATGAGAAT GACTGGAAACCGTACCGCATGCGGTGCCTATGGTAGCGGA GCTTCACATGGCTTCAG ACCAACAGCCTAT Contact DG for more information
sequence-based reagent	inx8_delta.F	this work		CCTTCGACCTGATTT CCCCTTCTTCTAATG Contact DG for more information

sequence-based reagent	inx8_delta.R	this work		CTATTGCTTTCCGTT CTTCAAGATGTTGTTG Contact DG for more information
sequence-based reagent	inx8_RPR	this work		GGTGGCCAATAAAAATGCTTTTCTTTTT GCTTTTCTCTATCTA CTTCCGTTCCGCCCC GGAGGTTGCCGTGG AGATGTACAGCGAC TTTTTAGTAAGTCTT TTCAAC Contact DG for more information
sequence-based reagent	inx8_sgRNA1.F	this work		TCTTGAGTGACTTGG TAGCATCGG Contact DG for more information
sequence-based reagent	inx8_sgRNA1.R	this work		AAACCCGATGCTACC AAGTCACTC Contact DG for more information
Recombinant DNA reagent (plasmid)	inx8_us_sgRNA1	this work		available upon request Contact DG for more information
sequence-based reagent	inx8_us_sgRNA1.F	this work		TCTTGTGGAAAACAG AGGAATGGG Contact DG for more information

sequence-based reagent	inx8_us_sgRNA1.R	this work		AAACCCCATTCCTCT GTTTTCCAC Contact DG for more information
sequence-based reagent	inx-14delF	this work		GATACGACGTGAGCA ATGGAACGTC Contact DG for more information
sequence-based reagent	inx-14delR	this work		CTTGGACTTGAAGT GAGAGTTGGAG Contact DG for more information
sequence-based reagent	sygl1-F	this work		ATCATCGAACCA TTGTCATCACGC Contact DG for more information
sequence-based reagent	sygl1-R	this work		TTTGCCTTGATCTC CAAGTGTTGC Contact DG for more information
Genetic reagent (*C. elegans*)	**AG400**	(Starich et al. 2020)	*fasn-1(av138[fasn-1::gfp]) I*	
Genetic reagent (*C. elegans*)	**CB190**	(Brenner 1974)	*unc-54(e190) I*	
Genetic reagent (*C. elegans*)	**CB1282**	(Hosono et al. 1982)	*dpy-20(e1282) IV*	
Genetic reagent (*C. elegans*)	**DG2506**	(Govindan et al. 2009)	*acy-4(ok1806) V; tnEx42[acy-4::gfp + rol-6(su1006)]*	
Genetic reagent (*C. elegans*)	**DG4959**	(this work)	*qIs154[lag-2p::MYR::tdTomato + ttx-3p::gfp] V; tnIs5[lim-7p::gfp + rol-6(su1006)] X*	Contact DG for more information

Genetic reagent (*C. elegans*)	**DG4977**	(this work)	*inx-14(ag17) I; qIs154[lag-2p::MYR::tdTomato + ttx-3p::gfp] V; tnIs5[lim-7p::gfp + rol-6(su1006)] X*	Contact DG for more information
Genetic reagent (*C. elegans*)	**DG5020**	(this work)	*naIs37[lag-2p::mCherry::PH + unc-119(+)] I; bcIs39[lim-7p::ced-1::gfp + lin-15(+)] V*	Contact DG for more information
Genetic reagent (*C. elegans*)	**DG5026**	(this work)	*inx-14(ag17) naIs37[lag-2p::mCherry::PH + unc-119(+)] I; bcIs39[lim-7p::ced-1::gfp + lin-15(+)] V*	Contact DG for more information
Genetic reagent (*C. elegans*)	**DG5027**	(this work)	*naIs37[lag-2p::mCherry::PH + unc-119(+)] I; inx-9(ok1502) IV; bcIs39[lim-7p::ced-1::gfp + lin-15(+)] V*	Contact DG for more information
Genetic reagent (*C. elegans*)	**DG5029**	(this work)	*naIs37[lag-2p::mCherry::PH + unc-119(+)] I; inx-8(tn1513tn1555) inx-9(ok1502) IV; bcIs39[lim-7p::ced-1::gfp + lin-15(+)] V*	Contact DG for more information
Genetic reagent (*C. elegans*)	**DG5059**	(this work)	*inx-9(ok1502) IV*	Contact DG for more information
Genetic reagent (*C. elegans*)	**DG5063**	(this work)	*inx-8(qy78[mKate2::inx-8]) IV*	Contact DG for more information
Genetic reagent (*C. elegans*)	**DG5064**	(this work)	*inx-8(qy102(mKate2::inx-8)) inx-9(ok1502) IV*	Contact DG for more information

Genetic reagent (*C. elegans*)	**DG5070**	(this work)	*inx-14(ag17) I; inx-8(qy78[mKate2::inx-8]) IV*	Contact DG for more information
Genetic reagent (*C. elegans*)	**DG5131**	(this work)	*naIs37[lag-2p::mCherry::PH + unc-119(+)] I;inx-8(qy78[mKate2::inx-8]) IV; bcIs39[lim-7p::ced-1::gfp + lin-15(+)] V;*	Contact DG for more information
Genetic reagent (*C. elegans*)	**DG5133**	(this work)	*naIs37[lag-2p::mCherry::PH + unc-119(+)] I; inx-8(qy102(mKate2::inx-8)) inx-9(ok1502) IV; bcIs39[lim-7p::ced-1::gfp + lin-15(+)] V*	Contact DG for more information
Genetic reagent (*C. elegans*)	**DG5136**	(this work)	*sygl-1(q983[3xOLLAS::sygl-1]) naIs37[lag-2p::mCherry::PH + unc-119(+)] I; bcIs39[lim-7p::ced-1::gfp + lin-15(+)] V*	Contact DG for more information
Genetic reagent (*C. elegans*)	**DG5150**	(this work)	*inx-14(ag17) sygl-1(q983[3xOLLAS::sygl-1]) naIs37[lag-2p::mCherry::PH + unc-119(+)] I; bcIs39[lim-7p::ced-1::gfp + lin-15(+)] V*	Contact DG for more information

Genetic reagent (*C. elegans*)	**DG5181**	(this work)	*sygl-1(q983[3xOLLAS::sygl-1]) naIs37[lag-2p::mCherry::PH + unc-119(+)] I; inx-8(qy78[mKate2::inx-8]) IV; bcIs39[lim-7p::ced-1::gfp + lin-15(+)] V*	Contact DG for more information
Genetic reagent (*C. elegans*)	**DG5229**	(this work)	*naIs37[lag-2p::mCherry::PH + unc-119(+)] I; inx-8(qy78tn2031) IV; bcIs39[lim-7p::ced-1::gfp + lin-15(+)] V*	Contact DG for more information
Genetic reagent (*C. elegans*)	**DG5232**	(this work)	*naIs37[lag-2p::mCherry::PH + unc-119(+)] I; inx-8(tn2034) IV; bcIs39[lim-7p::ced-1::gfp + lin-15(+)] V*	Contact DG for more information
Genetic reagent (*C. elegans*)	**DG5248**	(this work)	*sygl-1(q983[3xOLLAS::sygl-1]) naIs37[lag-2p::mCherry::PH + unc-119(+)] I; inx-8(qy78tn2031) IV; bcIs39[lim-7p::ced-1::gfp + lin-15(+)] V*	Contact DG for more information
Genetic reagent (*C. elegans*)	**DG5249**	(this work)	*sygl-1(q983[3xOLLAS::sygl-1]) naIs37[lag-2p::mCherry::PH + unc-119(+)] I; inx-8(tn2034) IV; bcIs39[lim-7p::ced-1::gfp + lin-15(+)] V*	Contact DG for more information
Genetic reagent (*C. elegans*)	**DG5250**	(this work)	*inx-8(qy78tn2031) IV*	Contact DG for more information

Genetic reagent (*C. elegans*)	**DG5251**	(this work)	*inx-8(tn2034) IV*	Contact DG for more information
Genetic reagent (*C. elegans*)	**DG5270**	(this work)	*inx-14(ag17) I*	Contact DG for more information
Genetic reagent (*C. elegans*)	**DG5310**	(this work)	*naIs37[lag-2p::mCherry::PH + unc-119(+)] I; acy-4(ok1806) V; tnEx42[acy-4::gfp + rol-6(su1006)]*	Contact DG for more information
Genetic reagent (*C. elegans*)	**DG5320**	(this work)	*fasn-1(av138[fasn-1::gfp]) naIs37[lag-2p::mCherry::PH + unc-119(+)] I*	Contact DG for more information
Genetic reagent (*C. elegans*)	**DG5346**	(this work)	*naIs37[lag-2p::mCherry::PH + unc-119(+)] I; inx-8(qy78[mKate2::inx-8])/tmC5[tmIs1220] IV; bcIs39[lim-7p::ced-1::gfp + lin-15(+)] V*	Contact DG for more information
Genetic reagent (*C. elegans*)	**DG5347**	(this work)	*naIs37[lag-2p::mCherry::PH + unc-119(+)] I; inx-8(qy78tn2031)/tmC5[tmIs1220] IV; bcIs39[lim-7p::ced-1::gfp + lin-15(+)] V*	Contact DG for more information
Genetic reagent (*C. elegans*)	**DG5357**	(this work)	*tmC5[tmIs1220] inx-8(tn2075) IV*	Contact DG for more information

Genetic reagent (*C. elegans*)	**DG5366**	(this work)	*naIs37[lag-2p::mCherry::PH + unc-119(+)] I; inx-8(qy78[mKate2::inx-8])/tmC5[tmIs1220] inx-8(tn2075) IV; bcIs39[lim-7p::ced-1::gfp + lin-15(+)] V*	Contact DG for more information
Genetic reagent (*C. elegans*)	**DG5367**	(this work)	*inx-14(ag17) fasn-1(av138[fasn-1::gfp]) naIs37[lag-2p::mCherry::PH + unc-119(+)] I*	Contact DG for more information
Genetic reagent (*C. elegans*)	**DG5378**	(this work)	*fasn-1(av138[fasn-1::gfp]) naIs37[lag-2p::mCherry::PH + unc-119(+)] I; inx-8(qy78[mKate2::inx-8]) IV*	Contact DG for more information
Genetic reagent (*C. elegans*)	**DG5380**	(this work)	*bcIs39[lim-7p::ced-1::gfp + lin-15(+)] V*	Contact DG for more information
Genetic reagent (*C. elegans*)	**FX30140**	(Dejima et al. 2018)	*tmC5[tmIs1220] IV*	Contact DG for more information
Genetic reagent (*C. elegans*)	**JK1466**	(Francis et al. 1995)	*gld-1(q485)/dpy-5(e61) unc-32(e51) I*	Contact DG for more information
Genetic reagent (*C. elegans*)	**KLG006**	(Gordon et al., 2020)	*inx-8(qy78[mKate2::inx-8]) IV; tnIs6[plim-7::gfp + rol-6(su1006)] X; cpIs122(lag-2p::mNeonGreen::plcdeltaPH)*	Contact DG for more information

Genetic reagent (*C. elegans*)	**NK2571**	(Gordon et al., 2020)	*inx-8(qy78[mKate2::inx-8]); cpIs122 [lag-2p::mNeonGreen::plcdeltaPH]*	Contact DG for more information
Genetic reagent (*C. elegans*)	**NK2576**	(Gordon et al., 2020)	*inx-8(qy102(mKate2::inx-8)) inx-9(ok1502); cpIs122(lag-2p::mNeonGreen::plcdeltaPH)*	Contact DG for more information

1